Supporting information

All-inorganic halide perovskites for air-processed "n-i-p" monolithic perovskite/organic hybrid tandem solar cells exceeding 23 % efficiency

Sawanta S. Mali,[1] Jyoti V. Patil,[1,2] Julian A. Steele,[3,4] Mohammad Khaja Nazeeruddin,[5] Jin Hyeok Kim,[6] Chang Kook Hong*[1,2]

[1]*Polymer Energy Materials Laboratory, School of Chemical Engineering, Chonnam National University, Gwangju, Korea-61186

[2]Optoelectronic Convergence Research Center, School of Chemical Engineering, Chonnam National University, Gwangju, 61186, South Korea

[3]Australian Institute for Bioengineering and Nanotechnology, The University of Queensland, Brisbane, QLD 4072, Australia

[4]School of Mathematics and Physics, The University of Queensland, Brisbane, QLD, 4072, Australia

[5]Group for Molecular Engineering of Functional Materials Institute of Chemical Sciences and Engineering EPFL VALAIS 1951 Sion, Switzerland, Switzerland

[6]Department of Materials Science and Engineering, Chonnam National University, Gwangju South Korea-61186.

*Correspondence to: sawanta@jnu.ac.kr, sawantasolar@gamil.com (SSM); hongck@jnu.ac.kr (CKH)

Supplementary Figure S1| Schematic illustration of the synthesis of all-inorganic perovskite thin films by dynamic hot-air-assisted method.

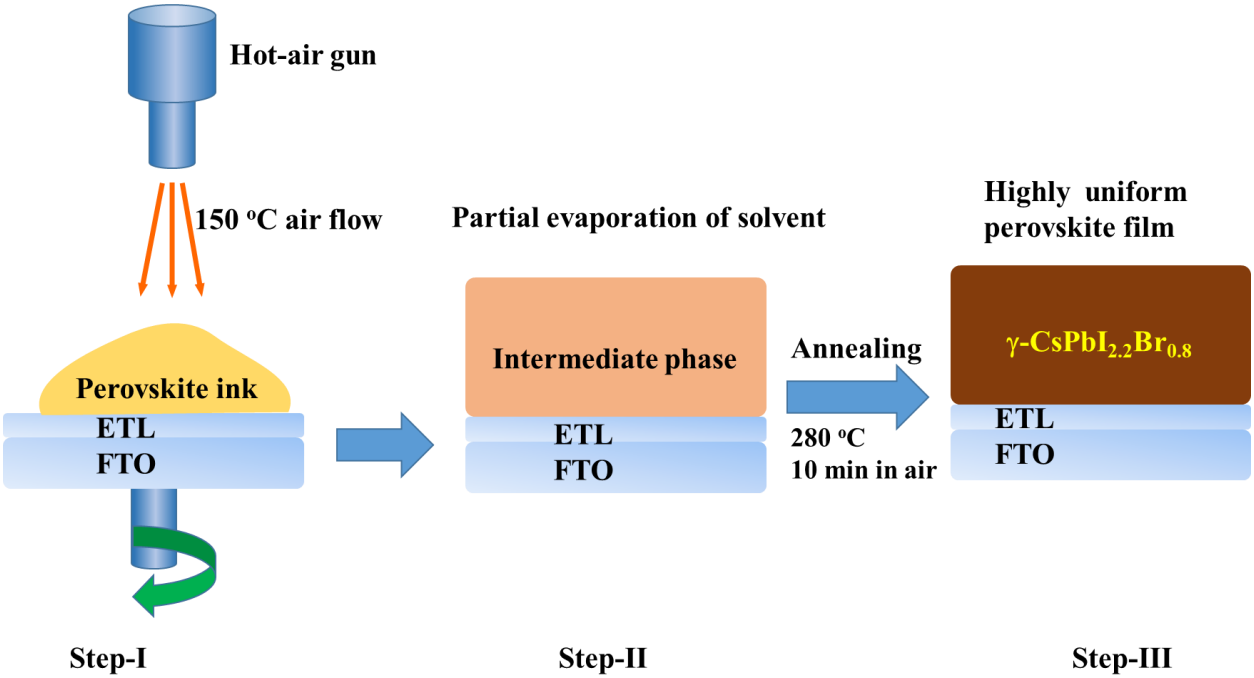

Supporting note S1: Experimental details for all-perovskite tandem solar cells

ITO (iTASCO, 10 Ωcm)-coated glass substrates were initially cleaned by sonicating in soap, water, ethanol, acetone, propanol, and then UV ozone treating for 20 min.

PTAA (poly[bis(4-phenyl) (2,4,6-trimethylphenyl)amine]) was coated by spin-coating from a 2mgml^{-1} solution in anhydrous toluene, at 5000rpm for 30s followed by annealing at 100 °C for 10 min.

PMMA (poly(methyl methacrylate)) was coated as a protecting layer by spin-coating a 0.2mg/ml solution in anhydrous acetonitrile (ACN), at 5000rpm for 20s, depositing the solution dynamically.

The 1.79 eV WBG perovskite front cells.

The precursor solution was prepared by mixing 0.45 M FAI, 0.3 M FABr, 0.15 M CsI, 0.1 M CsBr, 0.4 M $PbBr_2$ and 0.6 M PbI_2 in DMF/DMSO (4:1) to form $Cs_{0.25}FA_{0.75}PbI_{1.8}Br_{1.2}$ composition. The precursor solution was stirred at 60 °C for 24 h. After cooling to room temperature, the devices with a p–i–n structure were fabricated following a configuration of ITO/PTAA/PMMA/ WBG hybrid perovskite/C_{60}/BCP/Ag. The wide gap perovskite was deposited by spin-coating the solution at 4000rpm for 60s and 200 μL anhydrous methyl acetate used as an antisolvents. After finishing spinning, the film is then annealed at 100°C for 60min. Following deposition of the perovskite film, a thin (1nm) layer of lithium fluoride (LiF, iTASCO) was then deposited by thermal evaporation at a rate of 0.2Å/s. 25 nm of C_{60} (Lumtec) was then deposited by thermal evaporation at a deposition rate of 0.2Å/s for the first 10 nm and 0.5Å/s for the remaining 15 nm. For single junction wide bandgap cells, a 6 nm layer of bathocuproine (BCP, Lumtec) and 100 nm of silver were then deposited to finish the devices, both by thermal evaporation.

All-perovskite 2T tandem solar cells. For 2T tandem solar cells after deposition bottom ETL (i.e. 30 nm C_{60}, 2 nm BCP), nearly 25nm of AZO was then grown by atomic layer deposition in a NCD Lucida D100 ALD system at 85°C using trimethylaluminum (TMA), diethylzinc (DEZ), and water. Chamber and process nitrogen flows were set to 250 and 450 sccm, respectively. All precursors were unheated and pulsed off of room-temperature vapor pressures. The 25nm AZO film was deposited with of 3 cycles of Al_2O_3 followed by 12 supercycles of AZO; a single AZO supercycle consists of 19 cycles ZnO and 1 cycle Al_2O_3. The recipe used for both the Al_2O_3 and ZnO cycles proceeded by: a metalorganic (TMA or DEZ, respectively) pulse (0.2s), purge (5s), H_2O pulse (0.25s), and purge (5s). Our measured growth rates at 85°C for Al_2O_3 and AZO [19:1] are 1.1Å/cycle and 20Å/supercycle, respectively. Then 5 nm ITO were then deposited by sputtering.

Low conductivity Indium Zinc Oxide (IZO) was RF sputter deposited from a 2”x11” ceramic target (In:Zn=70:30) at room temperature in an Argon-Oxygen atmosphere (0.75vol.% O_2 in Argon) at a pressure of 5mTorr using a power of 100W.

ITO was RF sputtered from a ceramic source at room temperature and 25mTorr with Ar - 0.5% O_2 mixture flowing at 5sccm.

Next HTL for rear subcell PEDOT:PSS (Clevios P VP AI 4083, Heraeus) solution was filtered with a nylon filter (0.4 μm pore size) and spin coated in air at 5000 rpm for 20s followed by heating

at 150°C for 10min, after which substrates were immediately transferred into a nitrogen glovebox for low gap perovskite deposition. These samples were further annealed for next 10 min in order to remove the tress oxygen.

The 1.21 eV NBG CsFAMA perovskite rear subcells.

Narrow bandgap (1.21 eV) perovskite precursor solutions were prepared by dissolving 0.5 M FAI, 0.45 M MAI (methylammonium iodide) (Greatcell), 0.05M CsI, 0.5 M Tin (II) Iodide (Alfa Aesar, 99.999% beads), and 0.5 M PbI_2, to produce a 1.8 M solution of nominal composition $Cs_{0.05}MA_{0.45}FA_{0.5}Sn_{0.5}Pb_{0.5}I_3$, in anhydrous N,N-dimethylformamide (DMF, Sigma Aldrich) and Dimethylsulfoxide (DMSO, Sigma Aldrich) at a ratio of 3:1 by volume. Additionally, 0.05M of SnF_2 (Sigma) or 5 $mgmL^{-1}$ Sn-power was added to the solution to suppress oxidation of tin.[S1] Before deposition of NBG perovskite layer, glove box was cleaned and flushed with N_2-gas thoroughly. The NBG perovskite thin films were deposited by spin-coating the above solution at 5000 rpm for 60 s and 300 μL anhydrous ethyl (EA) acetate as an antisolvents was dripped at 20s. Films were then annealed at 100°C for 10 min. 30nm of C_{60} (Lumtec) was then deposited by thermal evaporation at a deposition rate of 0.2Å/s for the first 10nm and 0.5Å/s for the remaining 20nm. Devices were then finished by depositing a 6 nm layer of bathocuproine (BCP, Sigma-Aldrich) and 100 nm of either silver by thermal evaporation.

Supplementary Figure S2| a, Schematic diagram of conventional inverted "p-i-n" 2T monolithic all-perovskite tandem devices typically processed by ALD, sputtered ICLs and thermally evaporated C_{60}, BCP ETLs. **b,** Typical cross sectional SEM image of the inverted p-i-n 2T all-perovskite tandem solar cells. **c,** Stability of all-perovskite tandem solar cell stored in the glove box without encapsulation at room temperature.

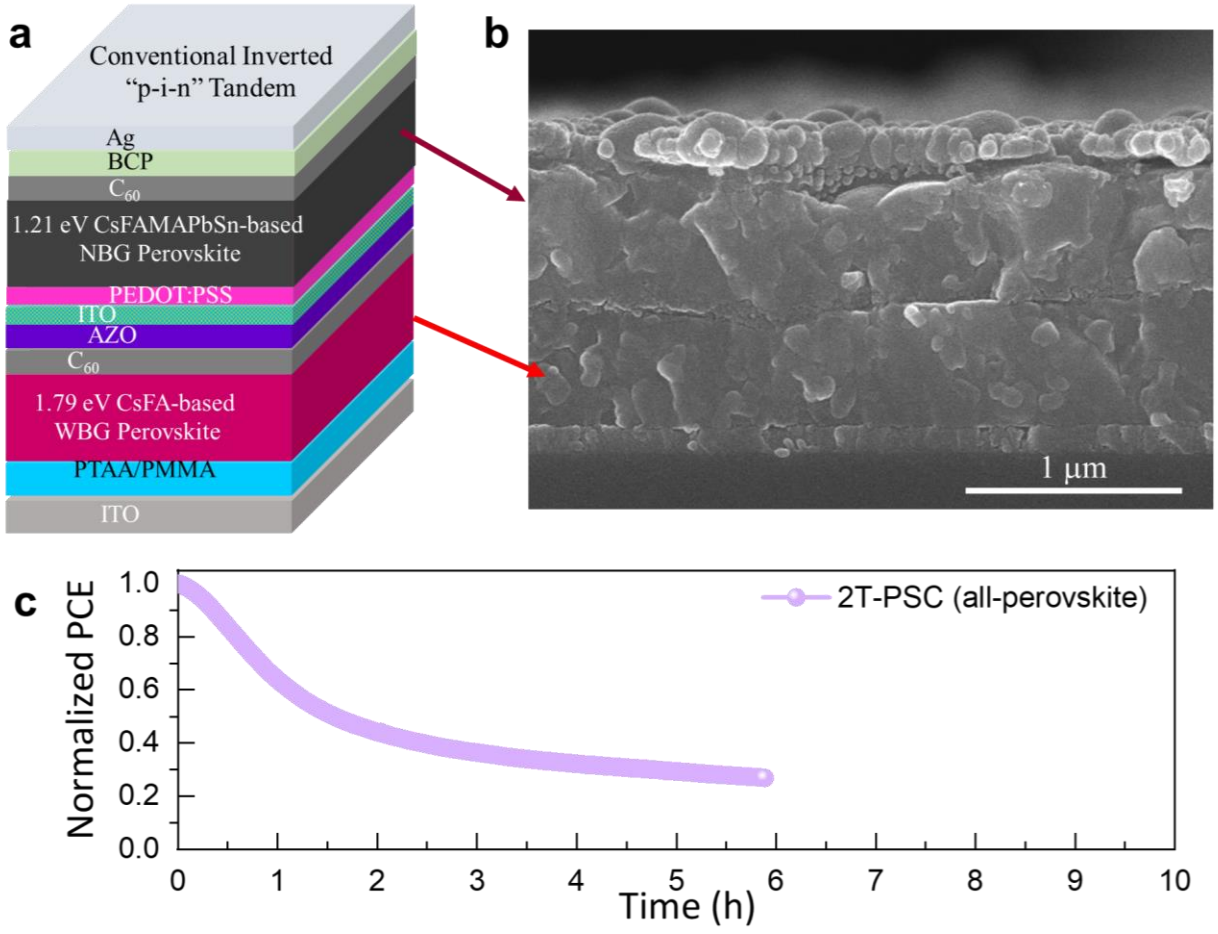

Supplemental Table S1. Summary of the device performance of the all-perovskite monolithic tandem solar cells.

Device configuration	**V_{OC} (V)**	**J_{SC} (mAcm^{-2})**	**FF (%)**	**PCE (%)**
ITO/HTL/WBG perovskite/ETL/ICL/NBG perovskite/ETL/Ag	1.907	14.32	71.36	19.48

Supplementary Figure S3| Single junction device open circuit voltage with respect to different band gap based on $CsPb(I_{1-x}Br_x)_3$ all-inorganic perovskite solar cells. Value taken as per previous literature. [S2]

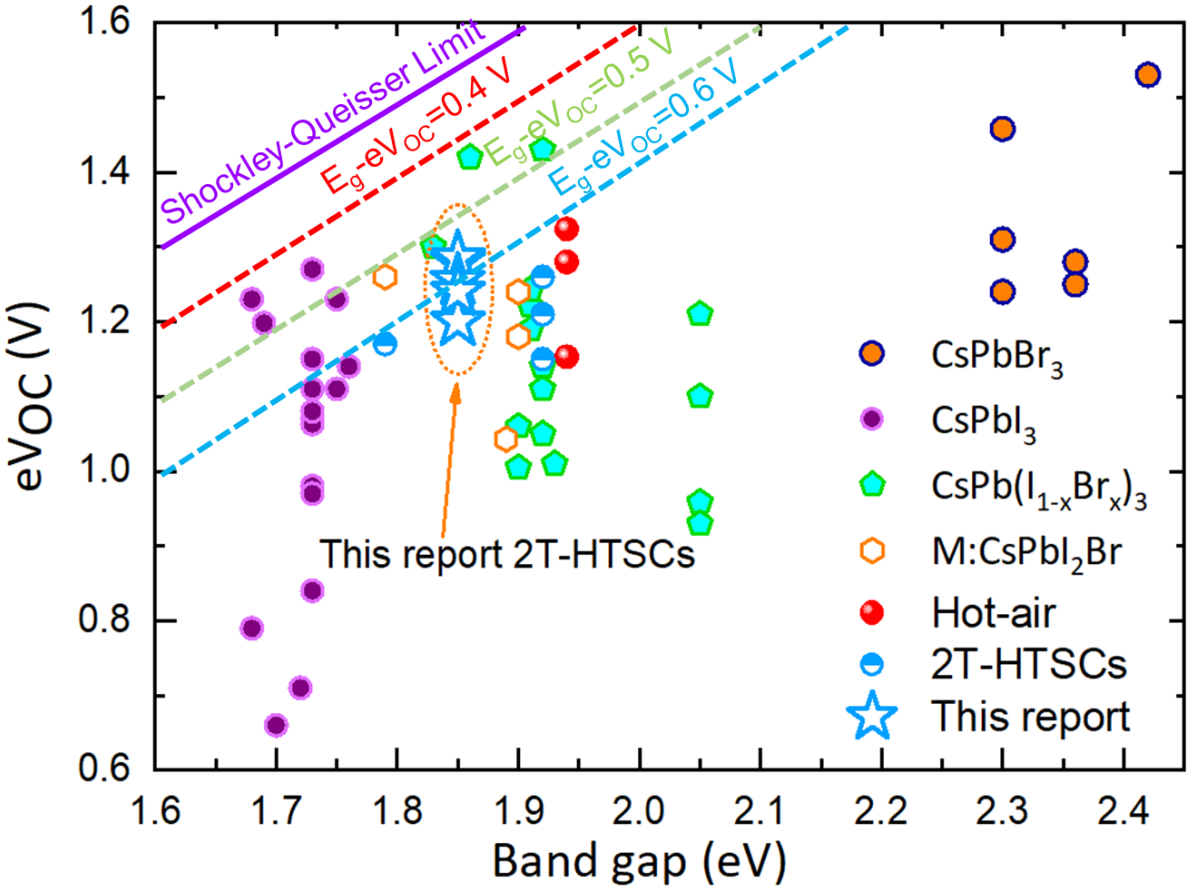

Supplementary Figure S4| a, Solubility test of PDIN crystals in methanol and 2,2,2-trifluoroethanol (TFE) solvents. **b,** Solution absorption spectrum of PDIN in TFE solvent.

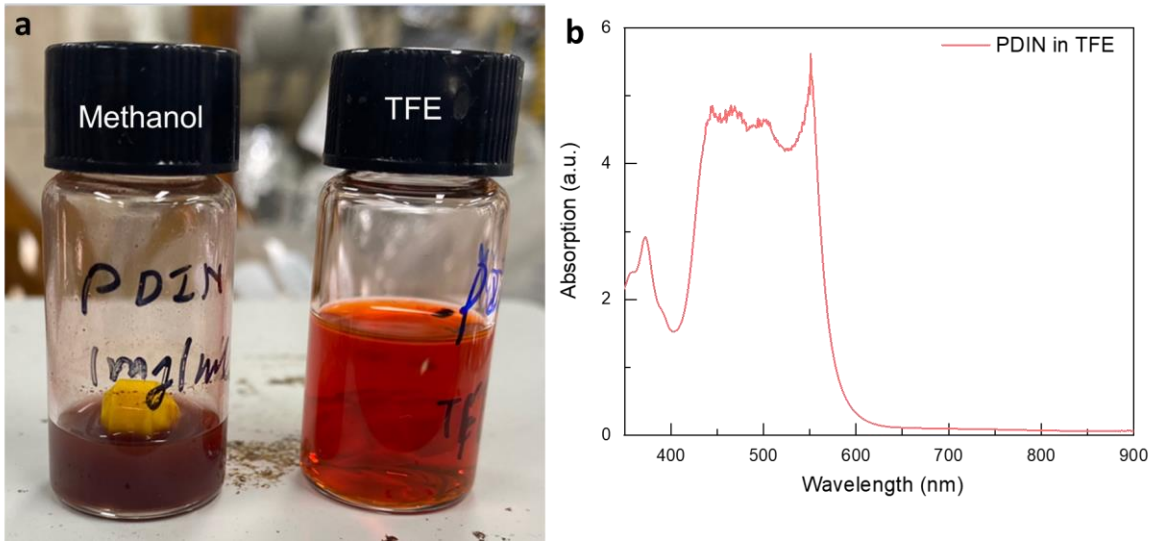

From the solubility test we observe that 2,2-trifluoroethanol (TFE) solvent is best for complete dissolution of PDIN crystals. The optical absorption also clears the good absorption with 2.33 eV band edge.

Supplementary Figure S5| UV-Vis absorption spectra of ZnO thin films before and after PDIN passivation.

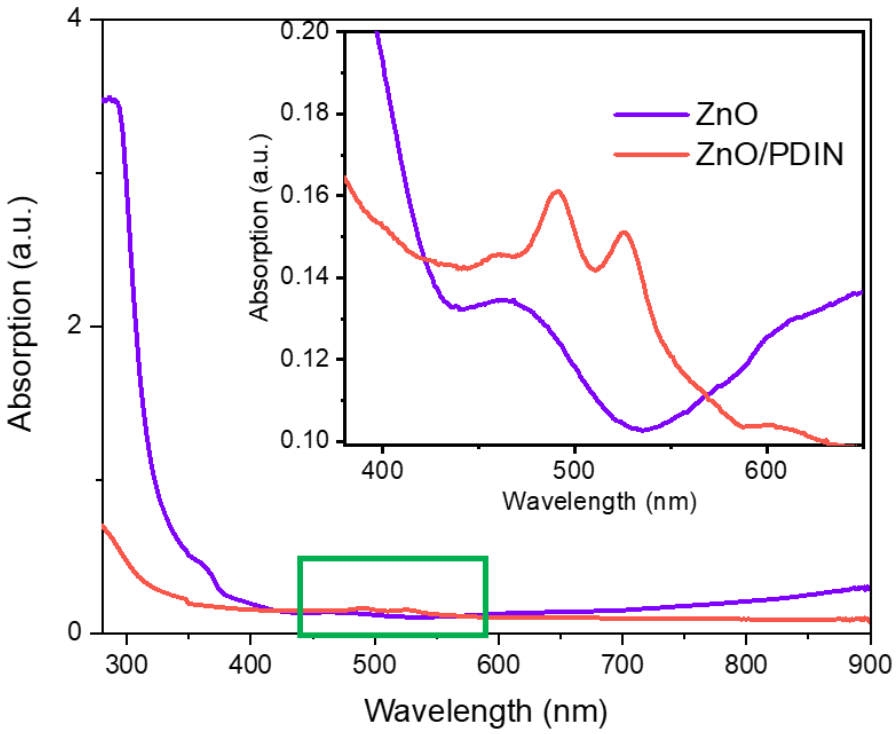

Supplementary Figure S6| Wettability, topographical and device properties. a, b, Water contact angle of the ZnO and ZnO/PDIN film on ITO substrate. **c,d** AFM images of ZnO thin films before and after PDIN passivation layer; **e,** molecular structure of the PDIN molecule.[S3] **f,** J-V characteristics of ZnO and ZnO/PDIN ETL-based IOPV devices.

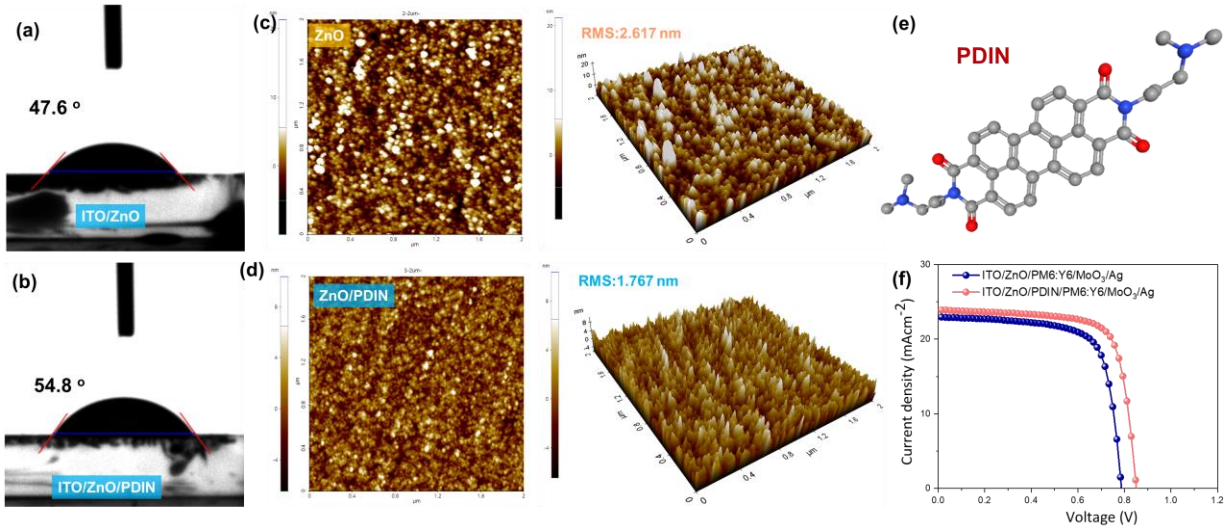

Supplementary Figure S7| a-c, XPS core level spectra of ZnO and ZnO/PDIN samples. **d,** Ultraviolet photoelectron spectroscopy (UPS) survey spectra (using the He-I line with photon energy of 21.22 eV). **e,** Magnified cutoff (E_{cutoff}) energy regions, **f,** valence band region (VBM) onset regions of the ZnO and ZnO/PDIN thin films deposited on ITO substrate with respect to the Fermi energy (E_F). **g,** Corresponding energy level diagram of each layer calculated from UPS analysis.

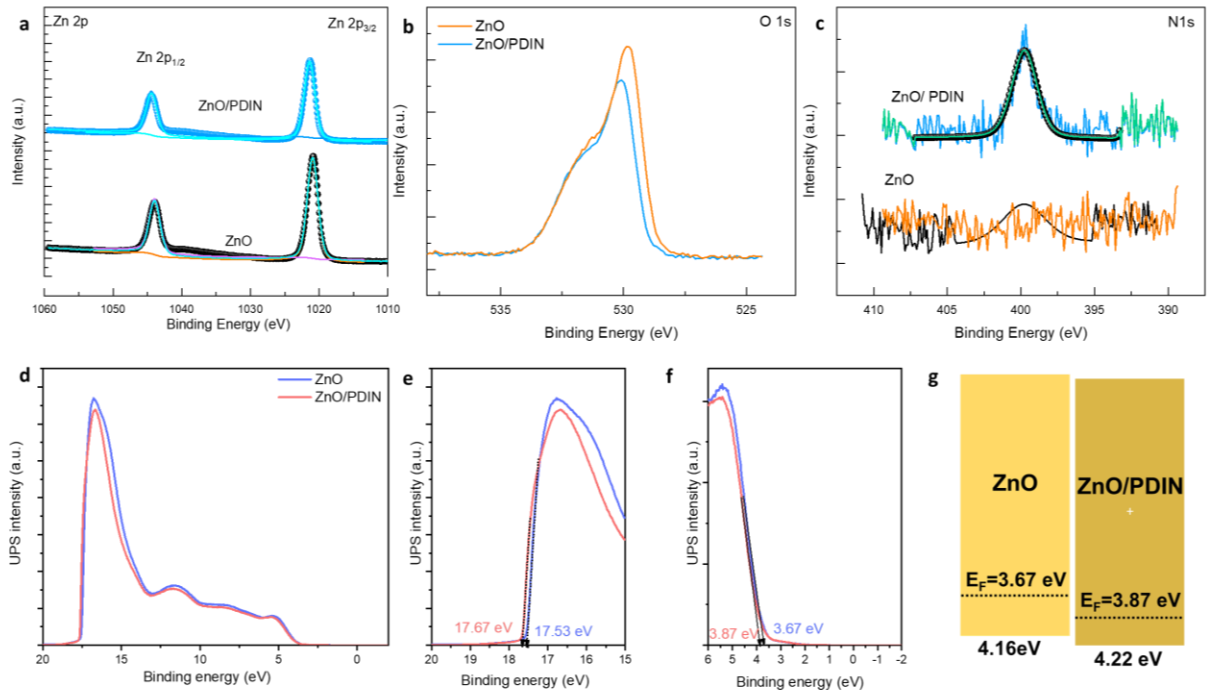

Supplementary Figure S8| Photovoltaic characteristics of top organic solar cell. a, Device architecture used in the ternary inverted organic top cells, where the ZnO/PDIN is electron transporting layer and MoO_3 (~10 nm) is hole transport layer; **b,** the typical cross-sectional SEM image of the whole device; **c, e** surface topography and 3D AFM images of the ternary PM6:Y6:$PC_{61}BM$ BHJ thin film deposited on ZnO/PDIN ETL; **d, f** the typical J-V curves of the organic top cell in forward and reverse scan under AM 1.5 sun illumination.

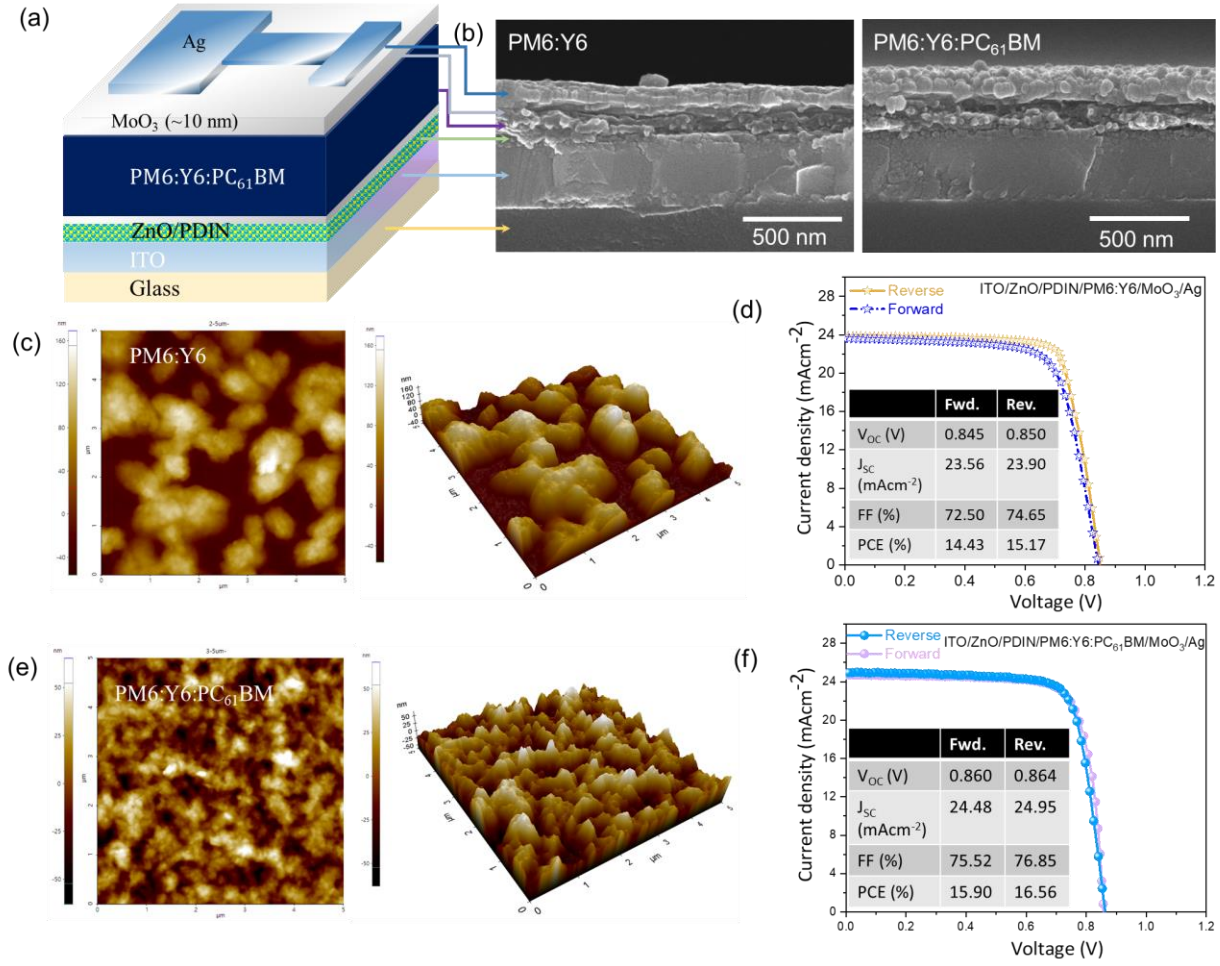

Supplementary Figure S9| a. Optical absorption spectrum of the donor PM6 and acceptors Y6, PCBM used in the ternary organic photovoltaic organic film deposited on ITO/ZnO/PDIN ETL substrate. **b.** EQE spectrum of the champion IOPV.

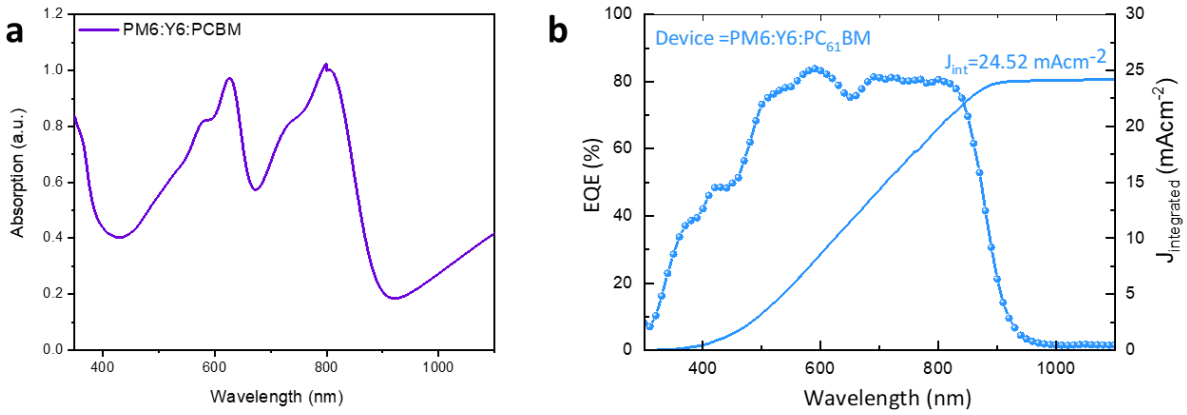

Supplementary Figure S10| Details of the statistical PV parameters of the IOPV-based cells. **a**, V_{OC}; **b,** J_{SC}; **c,** FF and **d,** Steady-state photocurrent density and stabilized power output (SPO) at maximum-power point tracking under working conditions with 100 mW cm^{-2} irradiation of the champion IOPVs**.**

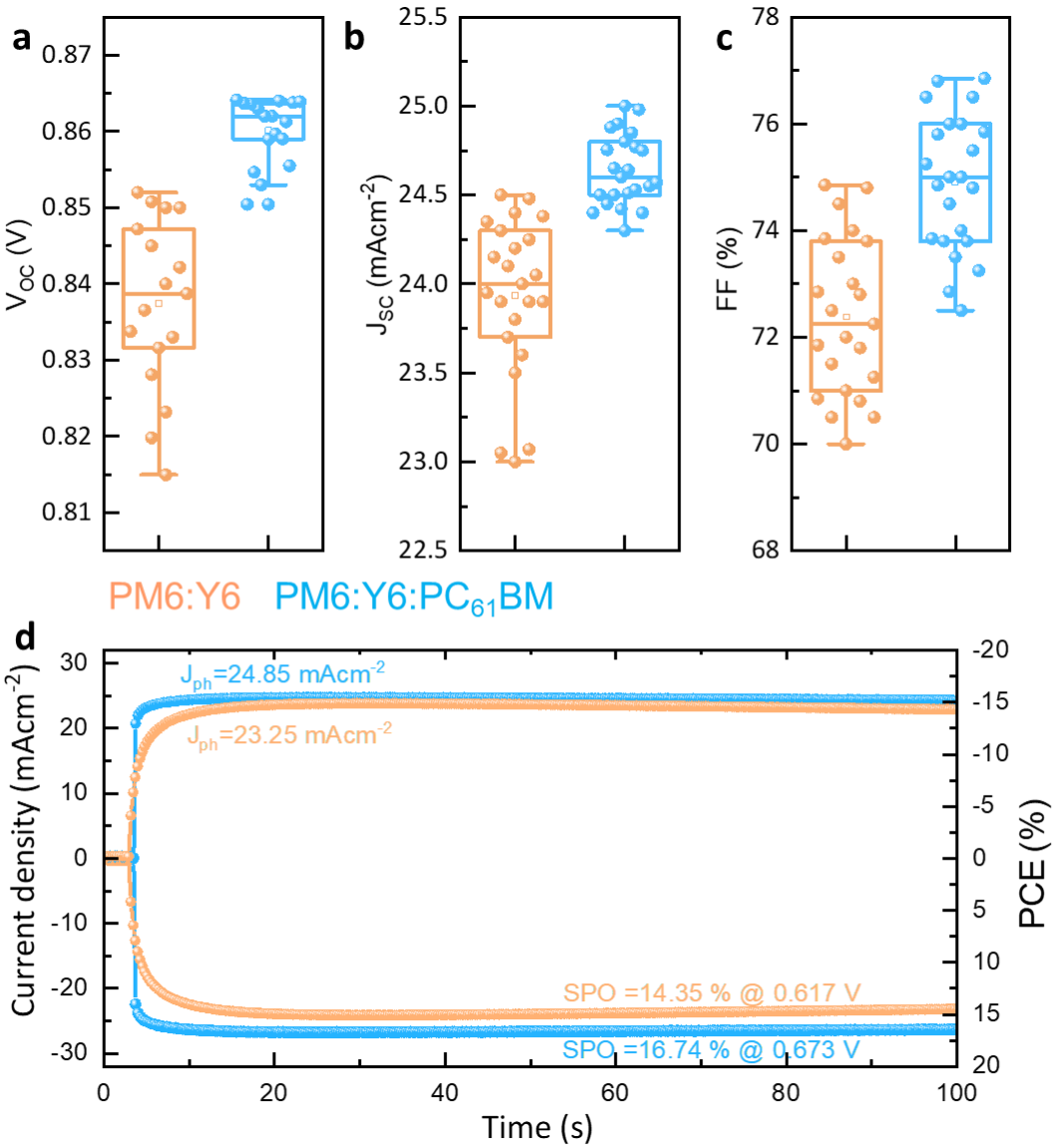

Supplemental Table S2. Summary of the device performance of the IOPV-based rear subcells with PDIN surface passivation. Device configuration is ITO/ZnO/PM6:Y6/MoO_x/Ag and ITO/ZnO/PDIN/PM6:Y6/MoO_x/Ag.

Device configuration	**V_{OC} (V)**	**J_{SC} ($mAcm^{-2}$)**	**FF (%)**	**PCE (%)**
ITO/ZnO/PM6:Y6/MoO_x/Ag	0.790	23.00	71.19	12.93
ITO/ZnO/PDIN/PM6:Y6/MoO_3/Ag	0.850	23.90	74.65	15.17

Supplementary Figure S11| Long-term ambient stability of the normal OPV and IOPV devices based on binary and ternary photoactive layer. The devices without encapsulation were kept at room temperature in dry box Relative humidity inside dry box was ~10 %. Samples were taken outside for J-V analysis and immediately stored in dry box.

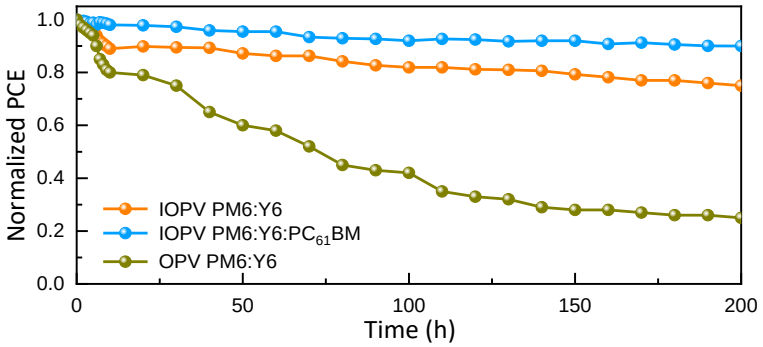

Supplementary Figure S12| Photographs of deposited perovskite thin films based on different metal ion dopants.

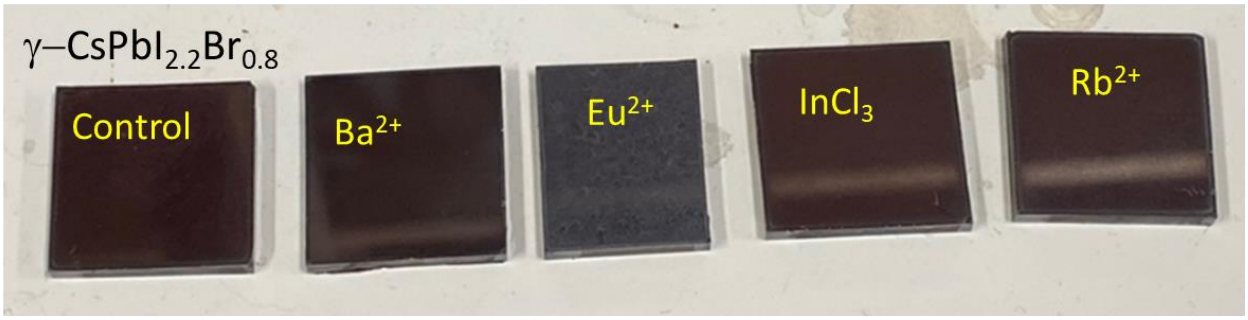

Supplementary Figure S13| Transmission and reflectance spectra of the γ–$CsPbI_{2.2}Br_{0.8}$-based bottom devices processed in ambient condition with different metal ion dopants.

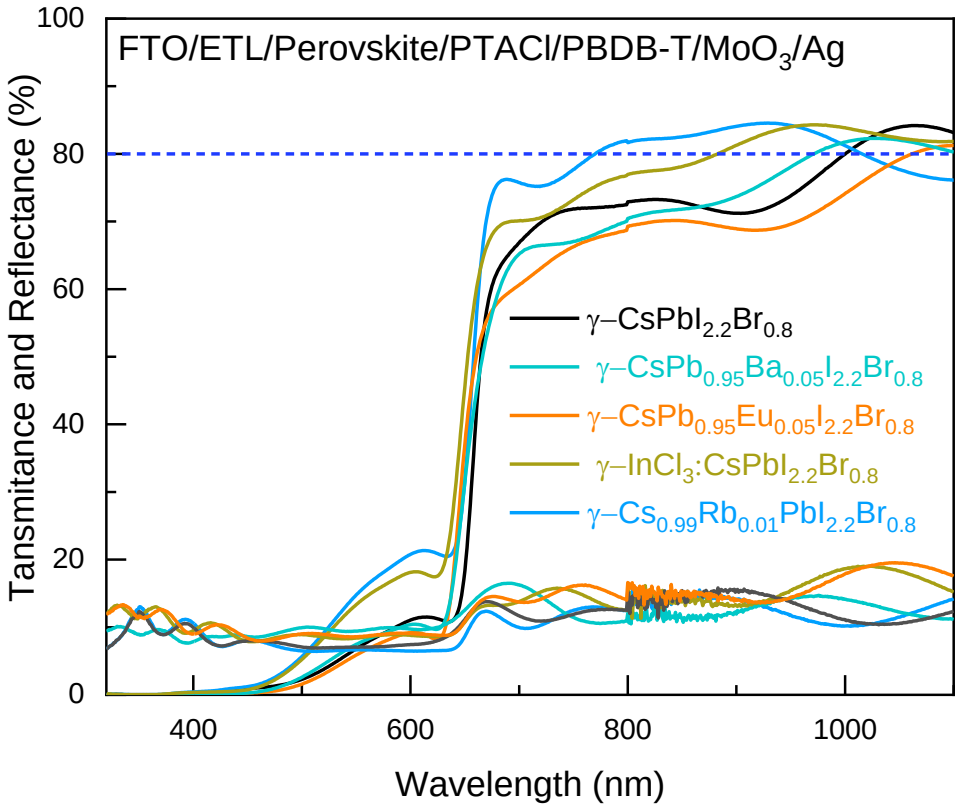

Supplementary Figure S14| Optical absorption characteristics of the bottom layer. a, Absorption spectra of all-inorganic wide-bandgap γ–$CsPbI_{2.2}Br_{0.8}$ perovskite films deposited on FTO/c-TiO_2/mp-TiO_2 substrates with and without PBDB-T HTL, showing no significant influence on its optical properties; **b,** Tauc plots of respective samples exhibiting an absorption onset at ~1.87 eV. The γ–$CsPbI_{2.2}Br_{0.8}$ and γ–$Cs_{0.99}Rb_{0.01}PbI_{2.2}Br_{0.8}$ films deposited exhibit the nearly same bandgap value. Linear fitting is used to calculate the bandgap values.

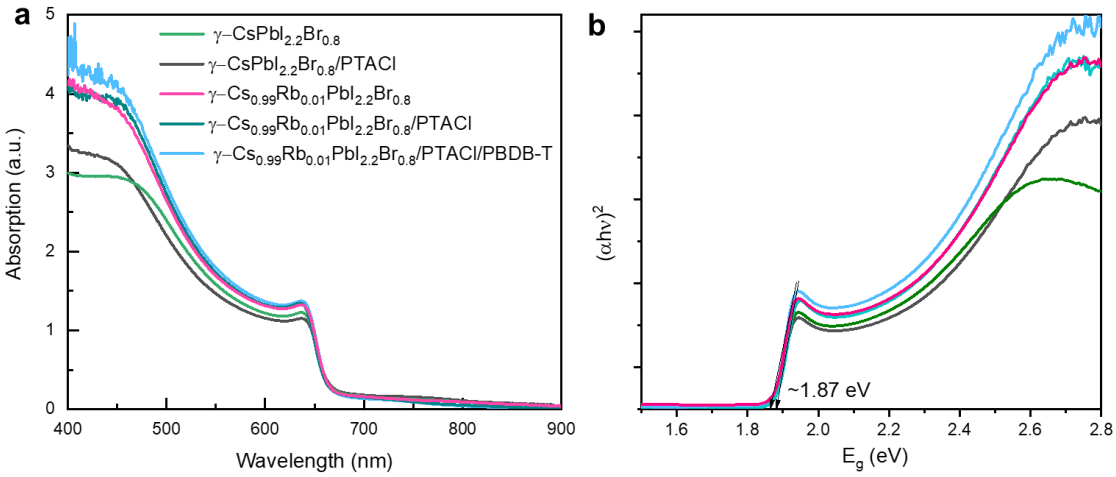

Detailed XRD refinement analysis

Analytical details and background: The whole XRD patterns were modeled using the La Bail method to understand the crystal phase, structural evolution, and take into account experimental artifacts (e.g. like 2theta offsets).

Confirmation of crystal structure:

From the analysis of the undoped γ-$CsPbI_{2.2}Br_{0.8}$ host, its crystal structure has been confirmed to be the γ-phase distorted cubic perovskite structure. As we did previous study via an evaluation of χ^2 values when modeling the structural data using the different α, β, and γ black phases.

Supplementary Figure S15| Comparison of the structural refinements made to XRD data recorded from black γ–$CsPbI_{2.2}Br_{0.8}$ thin film using the different symmetry perovskite unit cells to derive the fit. Their corresponding Chi-squared values are inset from highest (top) to lowest (bottom).

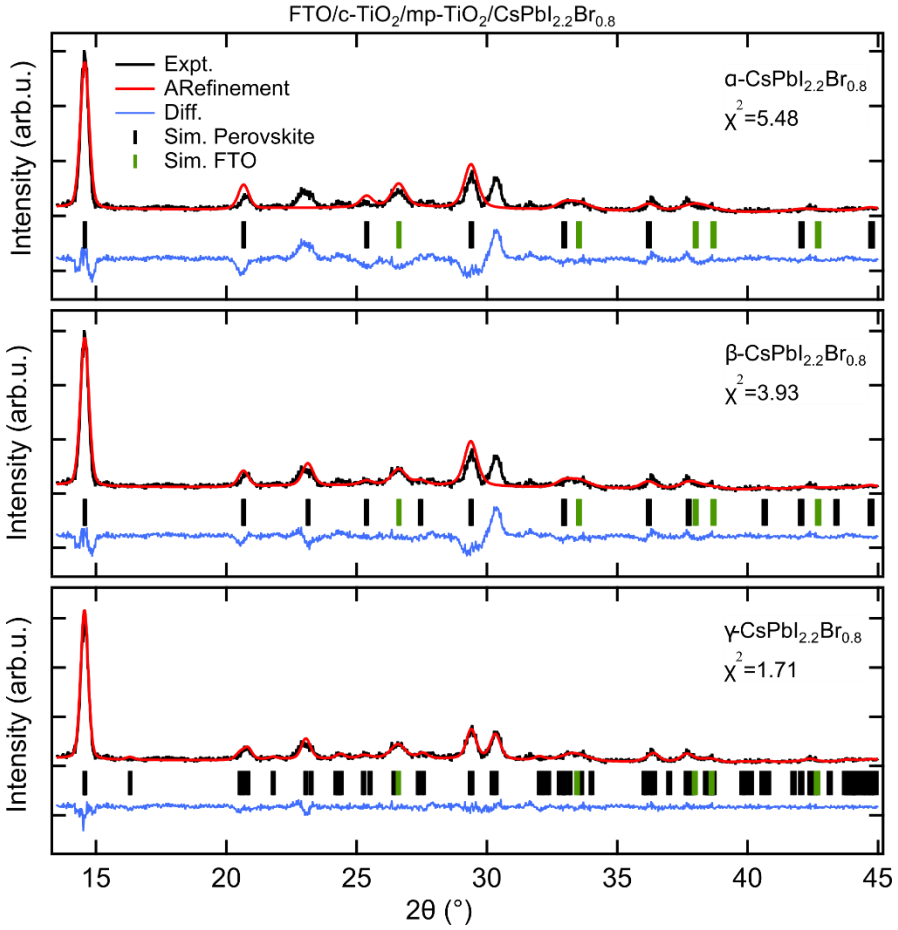

Phase stability of perovskites:

Supplementary Figure S16| Normalized XRD patterns and their structural refinements (La Bail method) of γ-phase $CsPbI_{2.2}Br_{0.8}$-based thin films with the derived lattice parameters inset.

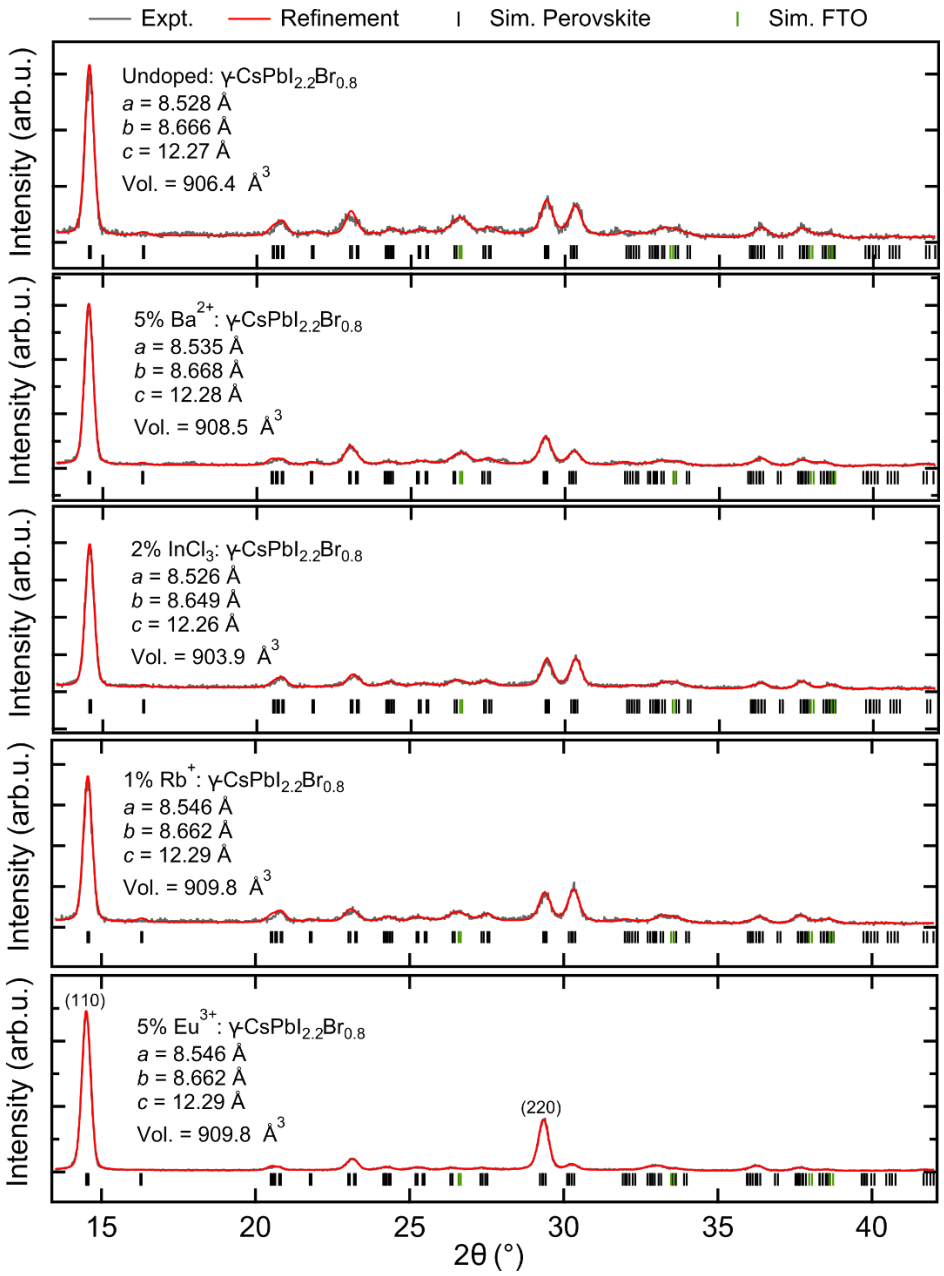

Supporting discussion: XRD

Similar structural refinements using a γ-phase crystal can be extended to the other doped forms of the perovskite thin films. Their corresponding unit cells are outlined above. Examining the XRD data recorded from the respective perovskite thin films, their scattering patterns do differ slightly. Along with some minor shifting in angle of some of the prominent perovskite peaks, there is some difference in the peak splitting. For the case of Eu^{2+} doping, the (110) and (220) peaks are relatively intense due to a relatively strong (110)-oriented tetragonal-type texture formation[S4] in the polycrystalline film. This orientation dependent feature in fact is verified, and accounted for, within the structural refinement modeled used in the FullProf program[S5].

The structural refinement of all doped materials leads to the data contained below:

Supplementary Figure S17| Normalized lattice parameters and calculated unit cell volume of the doped γ-$CsPbI_{2.2}Br_{0.8}$ perovskite thin films. The lines joining the data points are merely a guide for the eye.

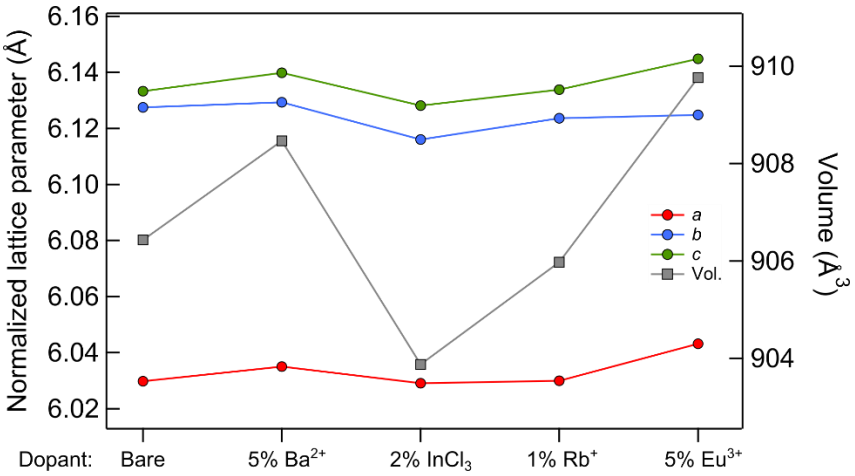

For the different dopants deployed here, even within the modest range of 1-5%, there are clear changes in the unit cell parameters and volume. This provides evidence of successful inclusion into the crystal lattice. Changes in crystal volume are directly linked to the changes in octahedral tilts and the γ-phase lattice distortions. Thus, **Figure S17** examines the changes in the crystal distortions and symmetry, relative to an undistorted cubic. We find that doping enacts a relatively large suppression of the spontaneous tetragonal strain formed in the distorted perovskite at RT. Through reducing the spontaneous strains a more stable perovskite structure can be realized[S6], i.e. become more tetragonal-like (β-phase). Further, there is a point of inflection for the role of dopants here, i.e. up unit 5 % doping the symmetry in monotonically improved, before this trend is reversed and begins to increase once more. These changes are also paralleled by an apparent saturation of the modified unit cell volume (**Figure S17**), echoing this restructuring inflection point.

Considering that tilting distortions of the perovskite structure are the underlying origin of instability, we can evaluate changes in the stability of the perovskite phase with respect to the development, or suppression, of the e_{tet} and e_{orth} strain components. Like the stabilizing effect of heating $CsPbI_3$ toward a thermodynamically stable cubic perovskite structure, we suggest that the this improvement in crystal symmetry will underpin gains to phase stability, arising due to a reversal of the spontaneous strains leading to phase decay.

For phase transitions in which the high symmetry α-phase is reduced to a degenerate γ-phase, the number of distortion components can be expressed in terms of symmetry-adapted strains. The degenerate symmetry-breaking distortions are thus divided into the tetragonal (e_{tet}) and orthorhombic (e_{orth}) strains, manifesting the β-phase and γ-phase, respectively. These quantities are calculated relative to an undistorted cubic unit cell, a_0, which is estimated by taking the cube root of the normalized unit cell volume. It follows that the spontaneous strain components are defined as: $e_1 = (a - a_0)/a_0$, $e_2 = (b - a_0)/a_0$ and $e_3 = (c - a_0)/a_0$, where a, b and c are the normalized

lattice parameters of the $CsPbI_{2.2}Br_{0.8}$-based orthorhombic phase. The separate strain components contributing to the lattice distortions are then given by: $e_{orth} = e_2 - e_1$ and $e_{tet} = (2e_3 - e_1 - e_2)/\sqrt{3}$. A factor of $\sqrt{3}$ is included here to ensure that the two strains are on the same scale.

Supplementary Figure S18| Decoupled orthorhombic (e_{orth}) and tetragonal (e_{tet}) spontaneous strain components for the different systems under investigation. The joining lines are merely a guide for the eye.

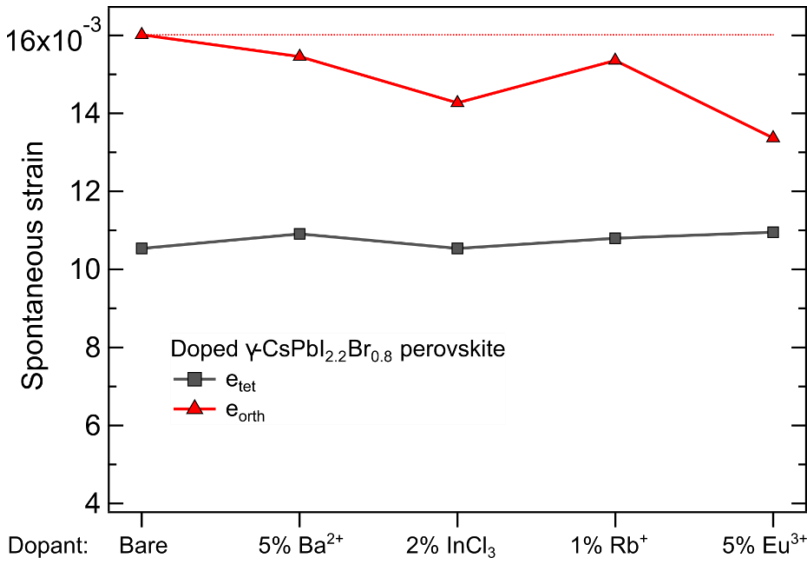

The decoupled strain components are presented in **Figure S18**. Starting of a bare γ-$CsPbI_{2.2}Br_{0.8}$ perovskite, all doping agents suppress the strain related distortions in the perovskite crystal, increasing its symmetry. Like the stabilizing effect of heating $CsPbI_{2.2}Br_{0.8}$ toward a stable cubic perovskite structure, we suggest that the doping-induced gain to phase stability arises due to a reversal of the spontaneous strains leading to phase decay. This effect is the largest for the Eu^{2+} system, which we find is the most stable when used in an ambient-stable device. Given the XRD data are recorded using a linear integration of the scattering pattern, the change in spontaneous strain and crystal symmetry may have shifted the final texture formation within the films, accounting for the large shift in relative intensity across different peaks.

Supplementary Figure S19| a. Photoluminescence (PL) and **b.** time-resolved PL (TRPL) analysis of (γ–$CsPbI_{2.2}Br_{0.8}$ and (γ–$Cs_{0.99}Rb_{0.01}PbI_{2.2}Br_{0.8}$) perovskite thin films before and after PTACl passivation. **a**, PL and **b**, TRPL spectra.

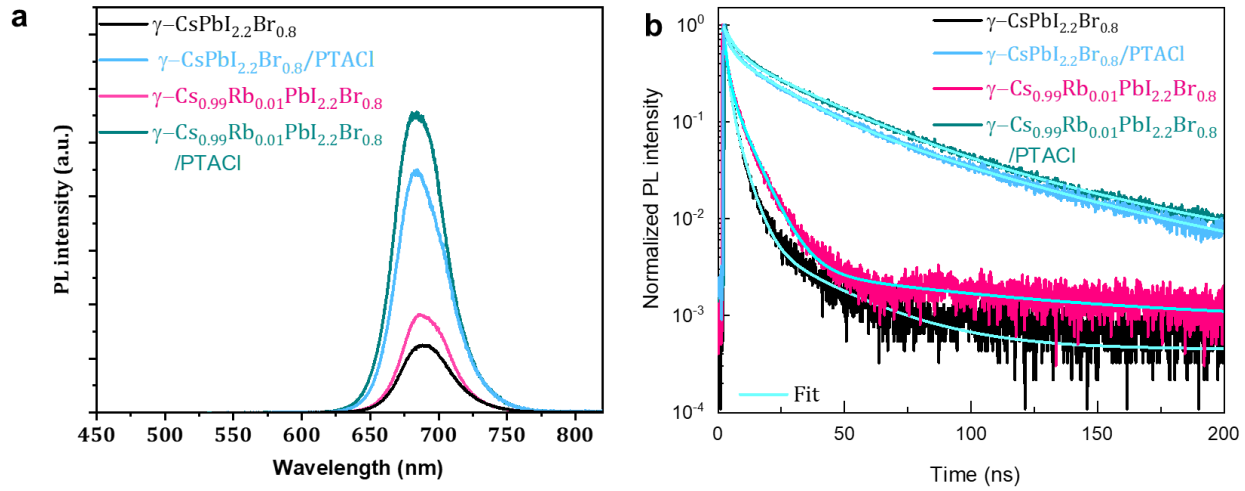

Supplemental Table S4. Summary of the PL lifetime parameters from fitting curves of the PL decay measurements.

Perovskite	**τ_1 (ns)**	**τ_2 (ns)**	**τ_3 (ns)**	**A_1***	**A_2***	**A_3***	**<τ> (ns)**
Glass/c-TiO_2/mp-TiO_2/γ–$CsPbI_{2.2}Br_{0.8}$	1.06	3.8	29	0.740	0.2564	0.006	6.2
Glass/c-TiO_2/mp-TiO_2/ γ–$Cs_{0.99}Rb_{0.01}PbI_{2.2}Br_{0.8}$	1.25	2.5	32	0.6967	0.2953	0.008	7.8
Glass/c-TiO_2/mp-TiO_2/γ–$CsPbI_{2.2}Br_{0.8}$/PTACl	3.20	20	59	0.4535	0.3833	0.1632	39.8
Glass/c-TiO_2/mp-TiO_2/γ–$Cs_{0.99}Rb_{0.01}I_{2.2}Br_{0.8}$/PTACl	3.58	15	63	0.5068	0.3054	0.1878	42.6

Supplementary Figure S20| The topography, and 3D AFM images of the γ–$CsPbI_{2.2}Br_{0.8}$ before and after PTACl passivation.

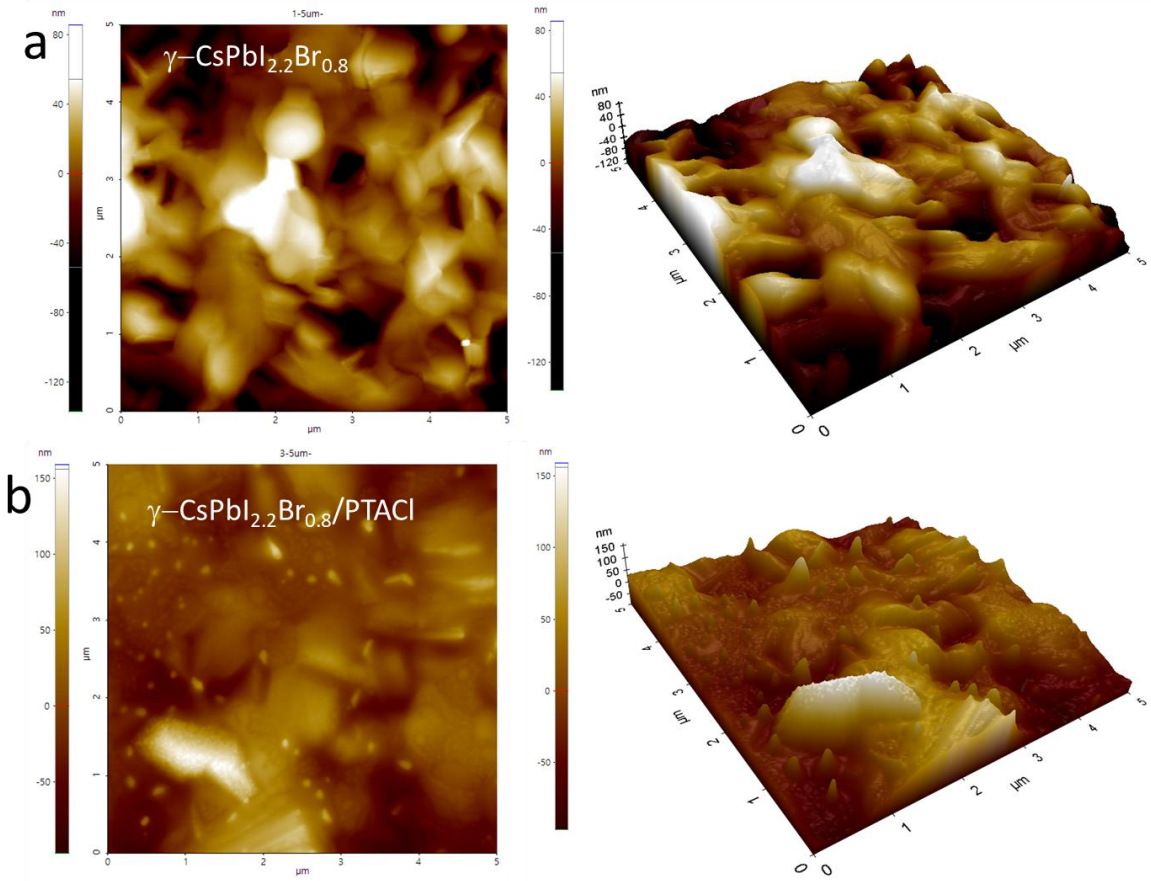

Supplementary Figure S21| The topography and hydrophobicity analysis. (a, b) 2Dand 3D AFM images of the γ–$Cs_{0.99}Rb_{0.01}PbI_{2.2}Br_{0.8}$ before and after PTACl/PBDB-T deposition. (c,d) **b,** Water contact angle of γ–$Cs_{0.99}Rb_{0.01}PbI_{2.2}Br_{0.8}$ perovskite films before and after PTACl passivation.

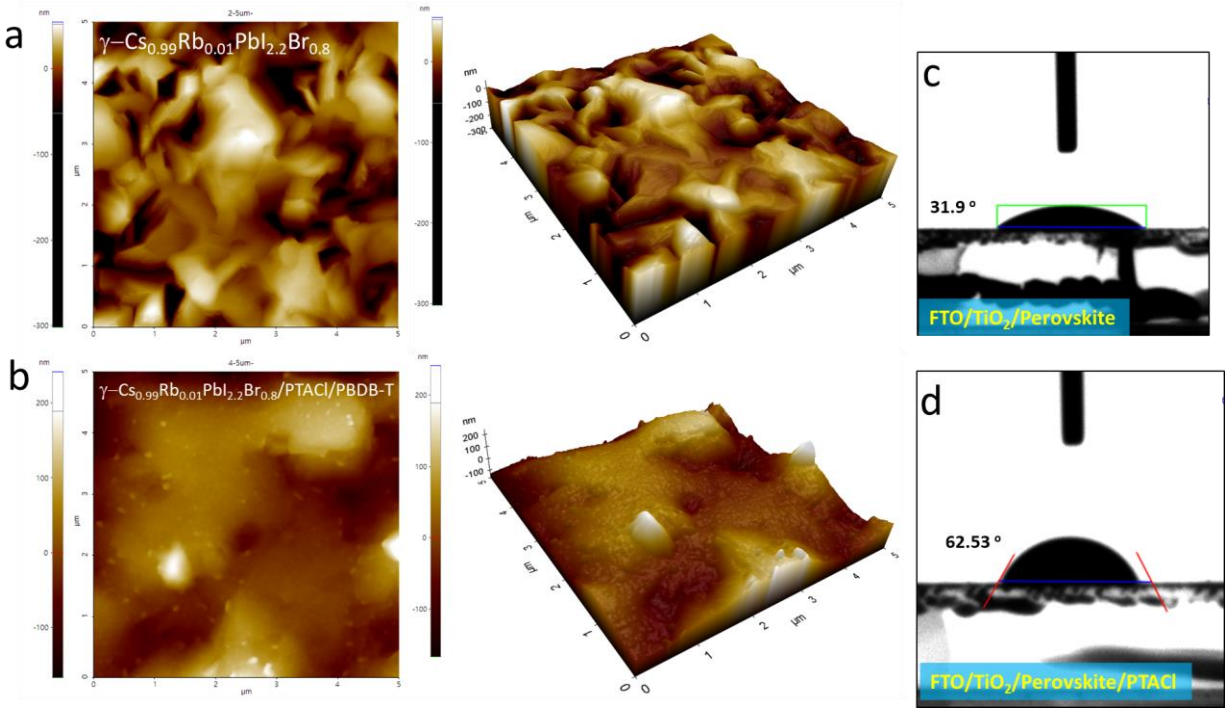

Supplementary Figure S22| Photovoltaic characteristics. **a**, Device architecture used in the all-inorganic perovskite front cells. **b**, Typical structure of PTACl passivation molecule used for surface passivation in the present study. **c-f,** Cross-sectional SEM images and the typical J-V curves of the control γ–$CsPbI_{2.2}Br_{0.8}$-based and γ–$Cs_{0.99}Rb_{0.01}PbI_{2.2}Br_{0.8}$-based single junction rear cells under AM 1.5 sun illumination.

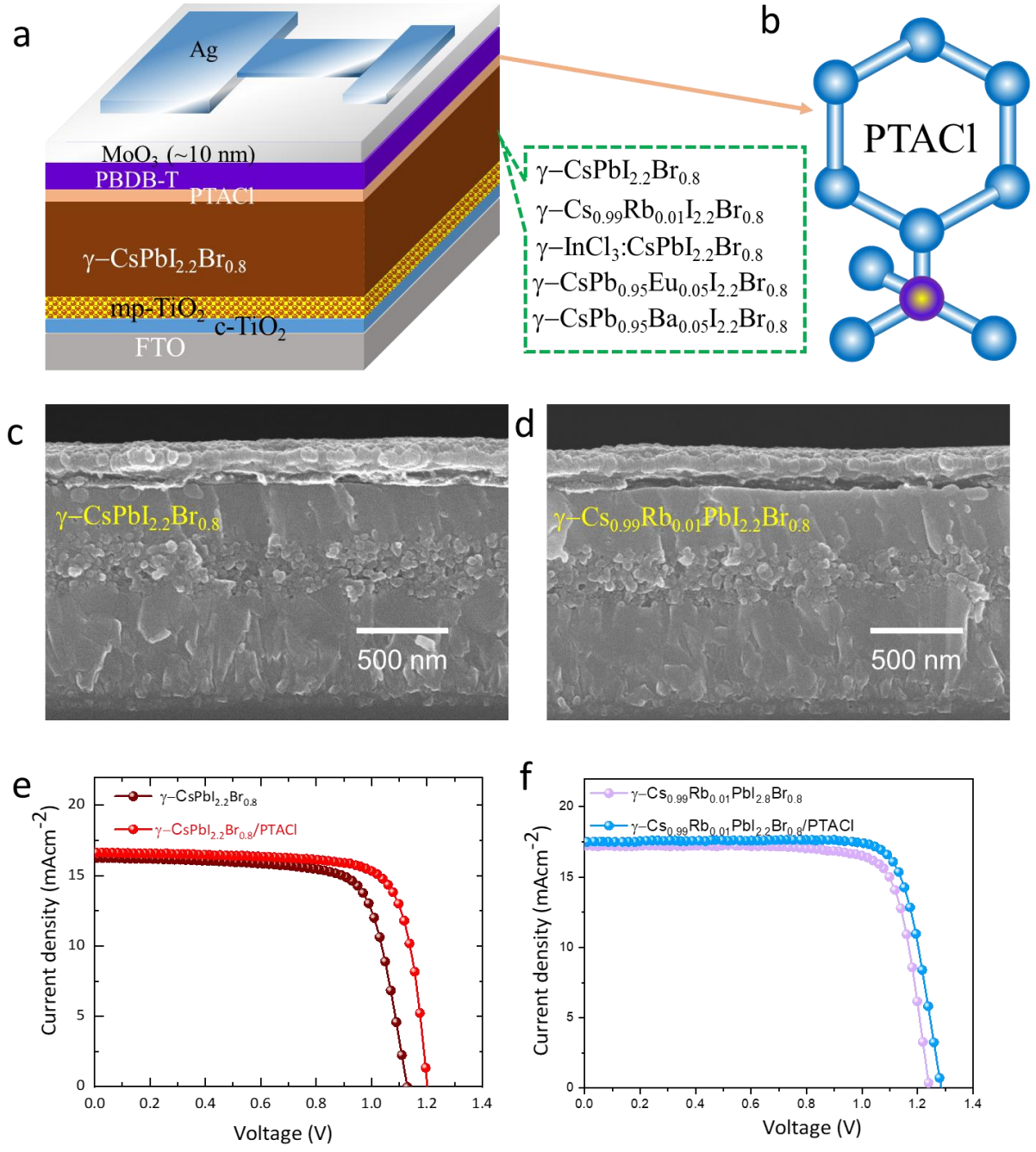

Supplementary Figure S23| Photovoltaic characteristics. a-c, Cross-sectional SEM images and **d-f,** the typical J-V curves of the γ–$InCl_3$:$CsPbI_{2.2}Br_{0.8}$, γ–$CsPb_{0.95}Eu_{0.05}I_{2.2}Br_{0.8}$ and γ–$CsPb_{0.95}Ba_{0.05}I_2Br_{0.8}$-based single junction rear cells under AM 1.5 sun illumination.

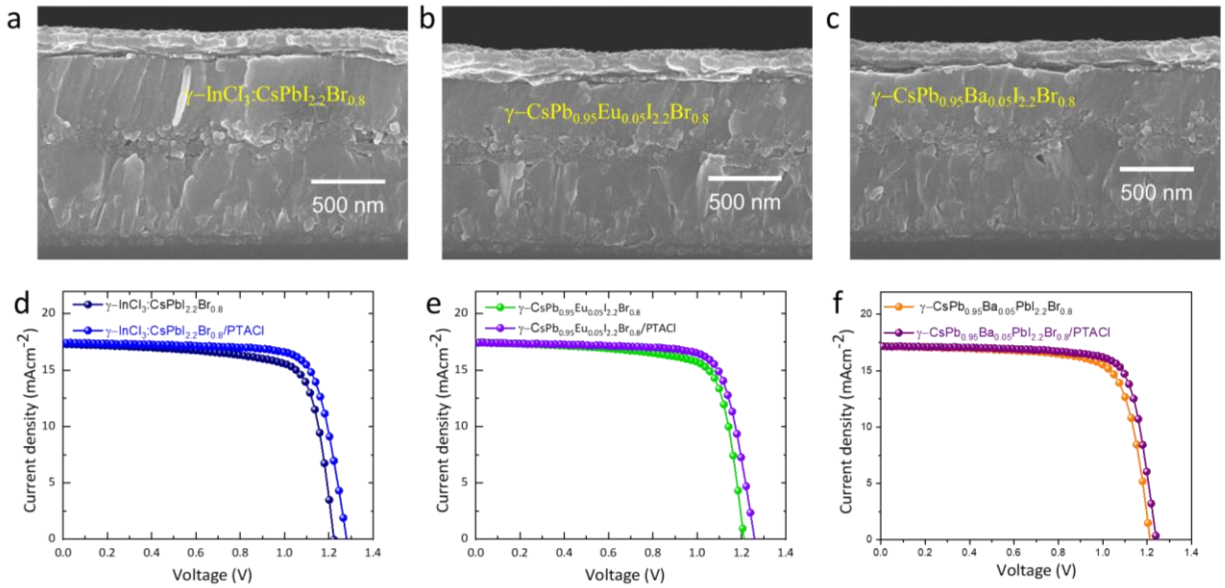

Supplemental Table S5. Summary of the device performance of the all-inorganic WBG-based front subcells with different dopants and PTACl passivation. Device configuration is FTO/c-TiO_2/mp-TiO_2/doped γ–$CsPbI_{2.2}Br_{0.8}$/PTACl/PBDB-T/MoO_3/Ag. *Here, ETL: c-TiO_2/mp-TiO_2; HTL: PBDB-T/MoO_3.*

Device configuration	**V_{OC} (V)**	**J_{SC} ($mAcm^{-2}$)**	**FF (%)**	**PCE (%)**
FTO/ETL/$CsPbI_{2.2}Br_{0.8}$/HTL/Ag	1.131	16.23	74.04	13.59
FTO/ETL/$CsPbI_{2.2}Br_{0.8}$/PTACl/HTL/Ag	1.200	16.68	75.45	15.10
FTO/ETL/$CsPb_{0.95}Eu_{0.05}I_{2.2}Br_{0.8}$/ HTL/Ag	1.211	16.47	74.8	14.92
FTO/ETL/$CsPb_{0.95}Eu_{0.05}I_{2.2}Br_{0.8}$/PTACl/ HTL/Ag	1.255	16.51	78.83	16.33
FTO/ETL/$CsPb_{0.95}Ba_{0.05}I_{2.2}Br_{0.8}$/ HTL/Ag	1.210	16.20	74.82	14.67
FTO/ETL/$CsPb_{0.95}Ba_{0.05}I_{2.2}Br_{0.8}$/PTACl/ HTL/Ag	1.240	16.20	77.65	15.60
FTO/ETL/$InCl_3$:$CsPbI_{2.2}Br_{0.8}$/ HTL/Ag	1.220	16.25	74.7	14.81
FTO/ETL/$InCl_3$:$CsPbI_{2.2}Br_{0.8}$/PTACl/ HTL/Ag	1.280	16.38	79.58	16.69
FTO/ETL/$Cs_{0.99}Rb_{0.01}PbI_{2.2}Br_{0.8}$/ HTL/Ag	1.239	17.20	77.70	16.56
FTO/ETL/$Cs_{0.99}Rb_{0.01}PbI_{2.2}Br_{0.8}$/PTACl/ HTL/Ag	**1.285**	**17.52**	**81.35**	**18.31**

Supplementary Figure S24| a, Ultraviolet photoelectron spectroscopy (UPS) survey spectra (using the He-I line with photon energy of 21.22 eV). **b,** Magnified cutoff (E_{cutoff}) energy regions, **c,** valence band region (VBM) onset regions of the γ–$Cs_{0.99}Rb_{0.01}PbI_{2.2}Br_{0.8}$ and γ–$Cs_{0.99}Rb_{0.01}PbI_{2.2}Br_{0.8}$/PTACl perovskite thin films deposited on FTO/c-TiO_2/mp-TiO_2 substrate with respect to the Fermi energy (E_F). **d, e**, Tauc plots and absorption spectra. **f**, Corresponding energy level diagram of each layer calculated from UPS analysis.

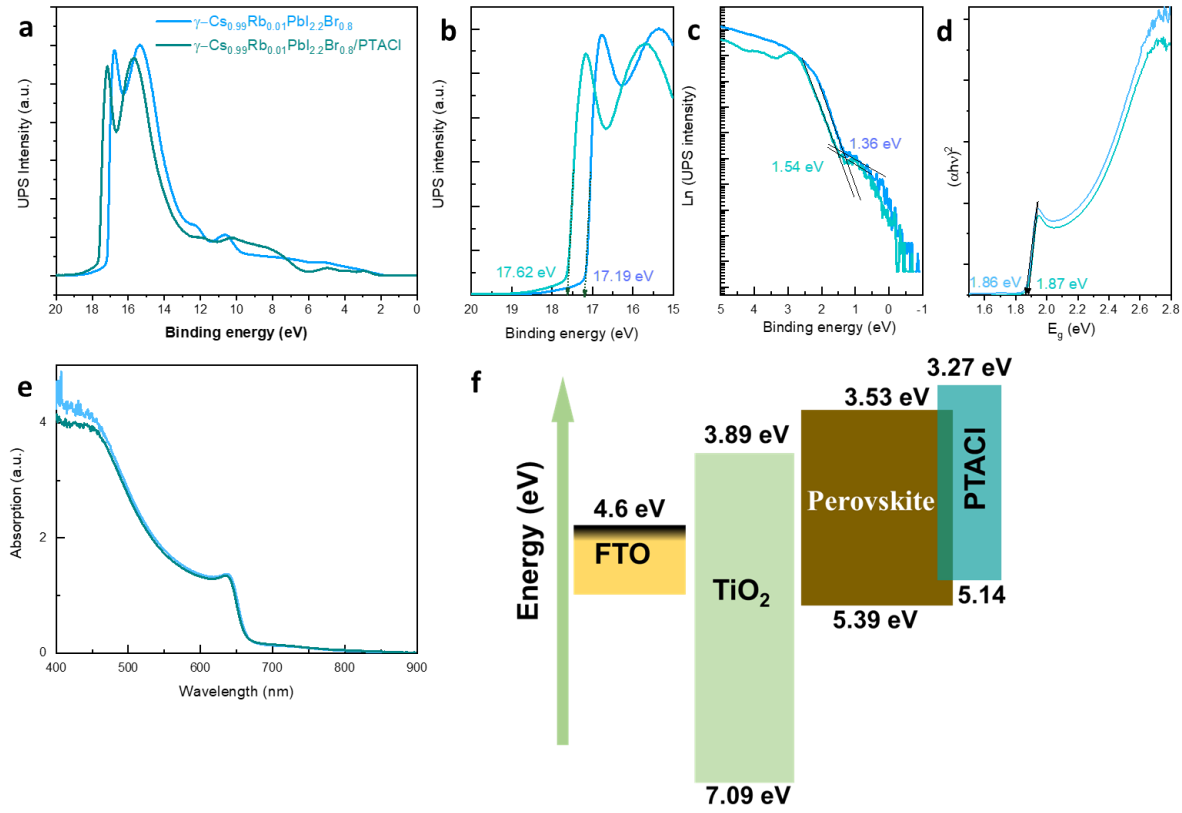

Supplementary Figure S25| Structural analysis of γ–$Cs_{0.99}Rb_{0.01}PbI_{2.2}Br_{0.8}$ perovskite thin films before and after PTACl passivation.

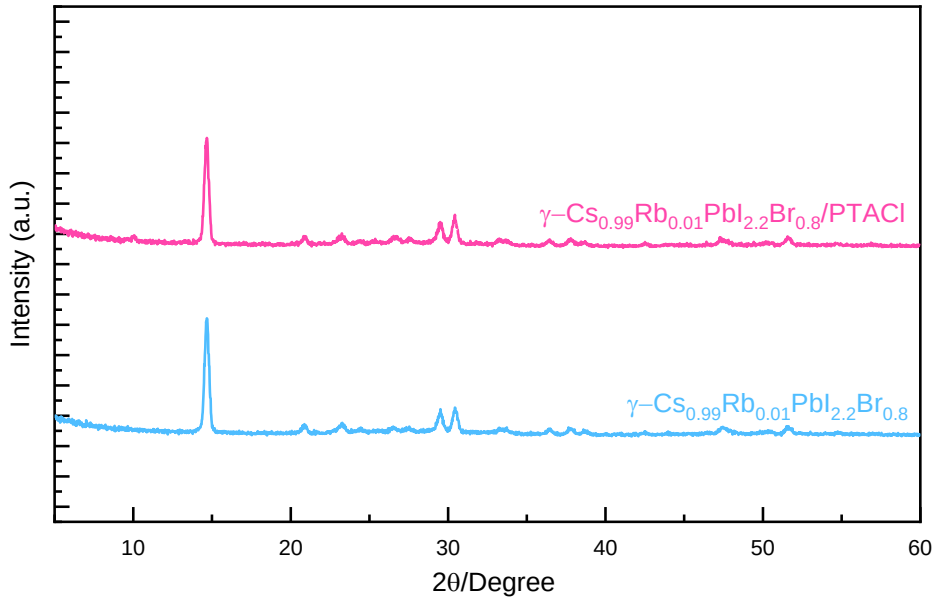

Supplementary Figure S26| XPS spectra of γ–$Cs_{0.99}Rb_{0.01}PbI_{2.2}Br_{0.8}$ and γ– $Cs_{0.99}Rb_{0.01}PbI_{2.2}Br_{0.8}$ /PTACl passivation.

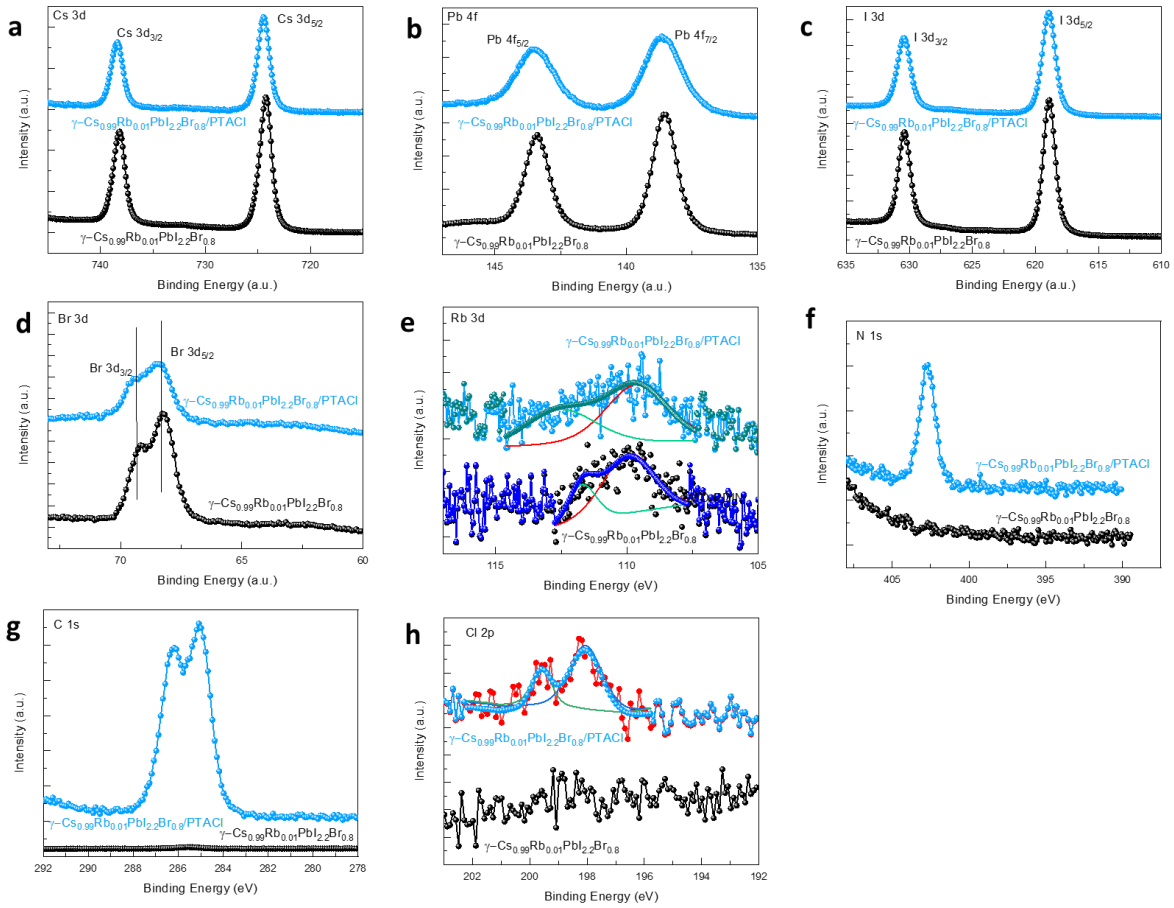

Supporting Note S2: Due to the interaction between PTA^+ and $Pb^{\delta+}$ cations and electron-donating nature, the $Pb^{\delta+}$ peak of the PTACl/γ–$Cs_{0.99}Rb_{0.01}PbI_{2.2}Br_{0.8}$ sample is shifted toward a lower binding energy, **Fig. S26b**. Together, this will facilitate the formation of a hydrophobic surface which terminates the degradation caused by moisture. The presence of PTACl organic cation of PTACl-$CsPbI_{2.2}Br_{0.8}$ sample has been confirmed from the appearance C1s, N1s and Cl2p core-level peaks appear after passivation, **Fig. S26e-g**.

Supplementary Figure S27| a, ToF-SIMS elemental depth profile of the PTACl-(γ−$CsPb_{0.99}Rb_{0.01}I_{2.2}Br_{0.8}$) perovskite film in positive polarity mode. **b-e**, Cross-sectional of cesium, lead, carbon and nitrogen elemental profile images of thin film measured by ToF-SIMS.

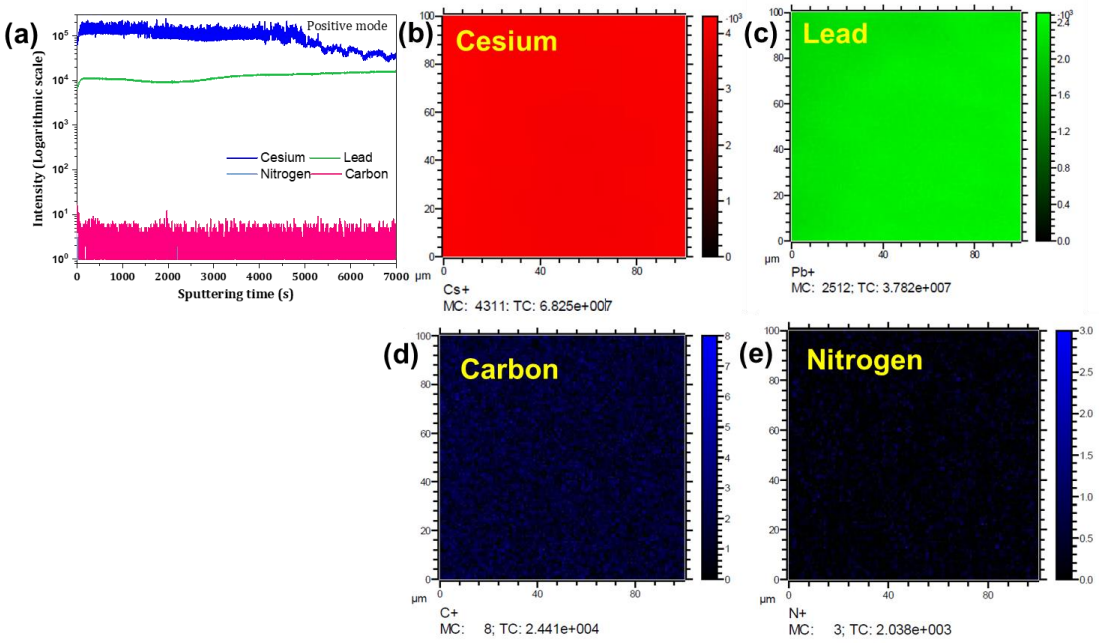

Supplementary Figure S28| a, ToF-SIMS elemental depth profile of the PTACl-(γ–$CsPb_{0.99}Rb_{0.01}I_{2.2}Br_{0.8}$) perovskite film in negative polarity mode. **b**, Cross-sectional of chlorine elemental profile image of thin film measured by ToF-SIMS. **c**, 3D render image Cl^- indicting PTACl is present only at the surface.

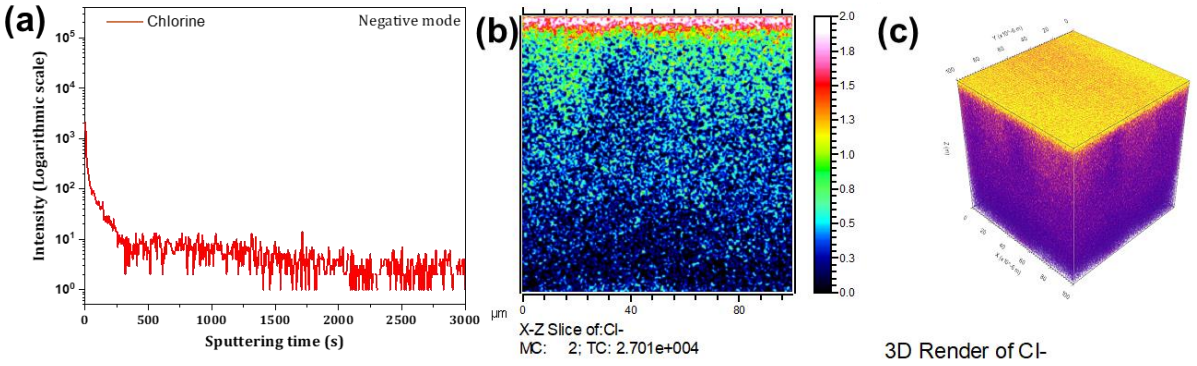

Supplementary Figure S29| a, Details of the statistical PV parameters of AI-PSC-based cells. **b,** EQE spectra of AI-PSCs based on γ–$CsPbI_{2.2}Br_{0.8}$ and γ–$Cs\,Rb_{0.01}PbI_{2.2}Br_{0.8}$ compositions. Long term stability of **c,** controlled and **d,** champion front subcells stored in ambient conditions without encapsulation. Relative humidity 35-45 %**.**

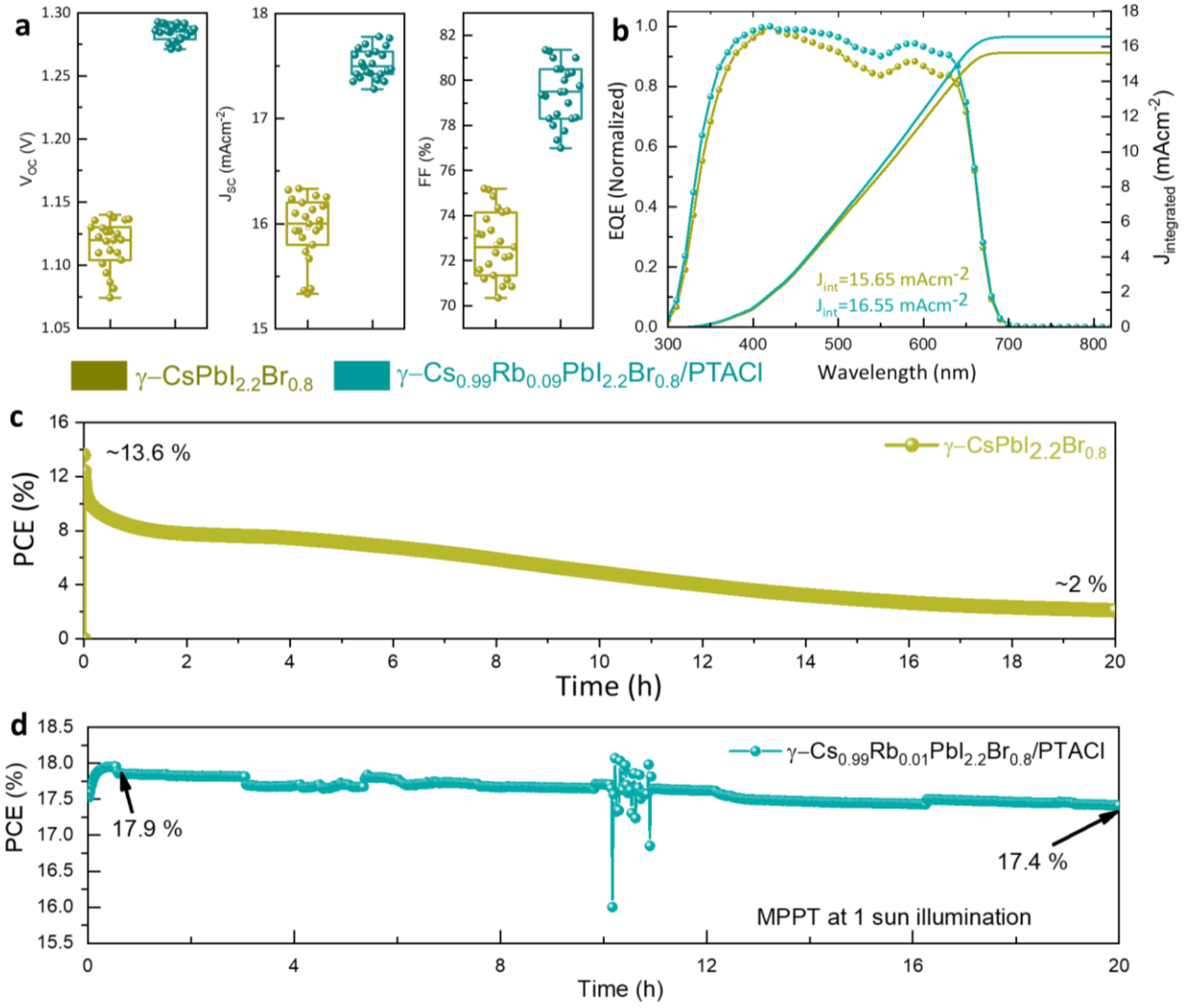

Supplementary Figure S30| FIB cross-sectional images of γ–$CsPbI_{2.2}Br_{0.8}$ and γ–$Cs_{0.99}Rb_{0.01}PbI_{2.2}Br_{0.8}$-based 2T-HTSCs recorded after 20 days aging.

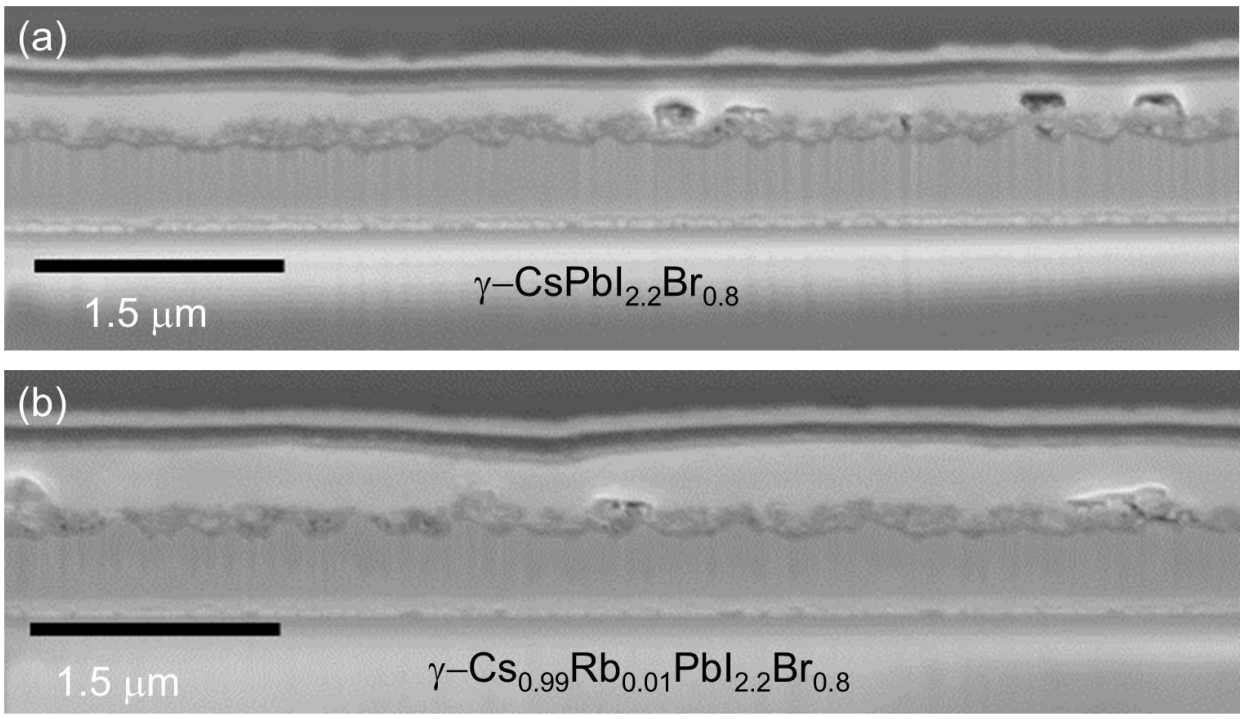

Supplementary Figure S31| ToF-SIMS elemental depth profile of the γ–$CsPbI_{2.2}Br_{0.8}$-based 2T-HTSC in negative polarity mode. ToF:SIMS recorded after 20 days aging.

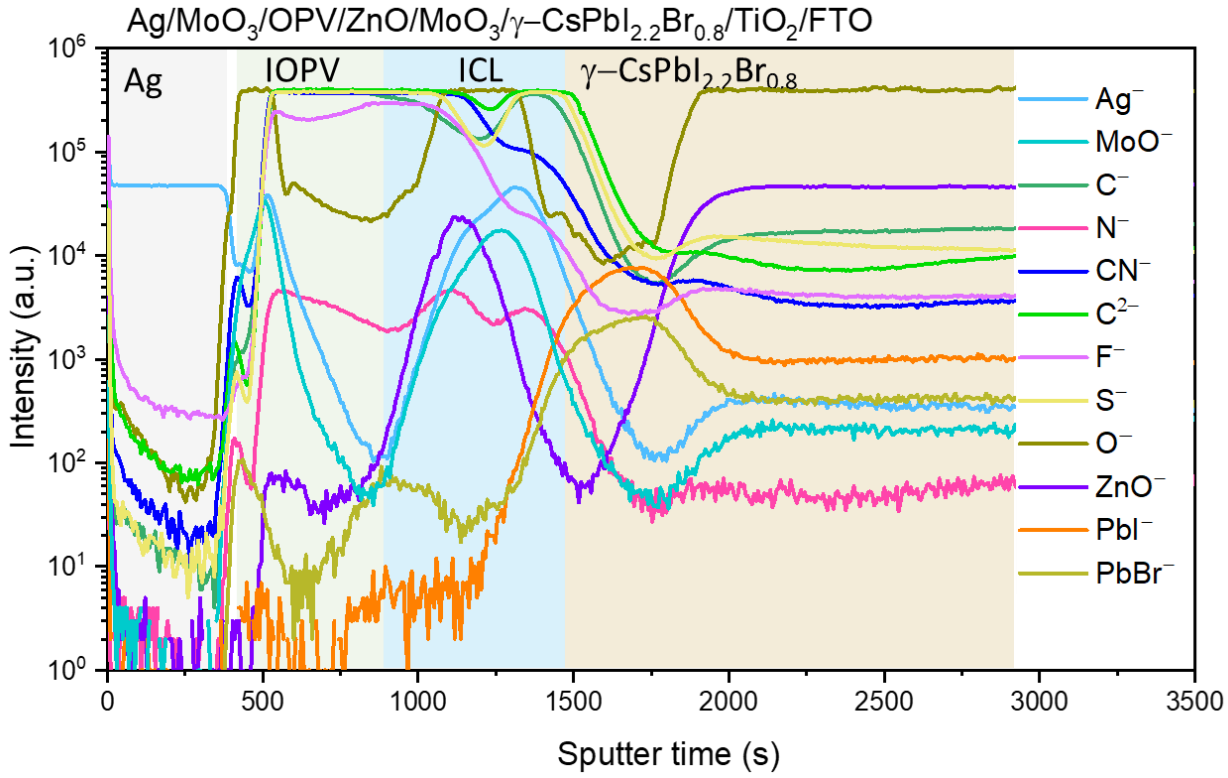

Supplementary Figure S32| Reconstructed 3D cross-sectional image profile showing separate silver, MoO_3, carbon, nitrogen, ZnO, lead iodide and lead bromide elemental layers of the γ–$CsPbI_{2.2}Br_{0.8}$-based 2T-HTSC device measured by ToF-SIMS. ToF:SIMS recorded after 20 days aging.

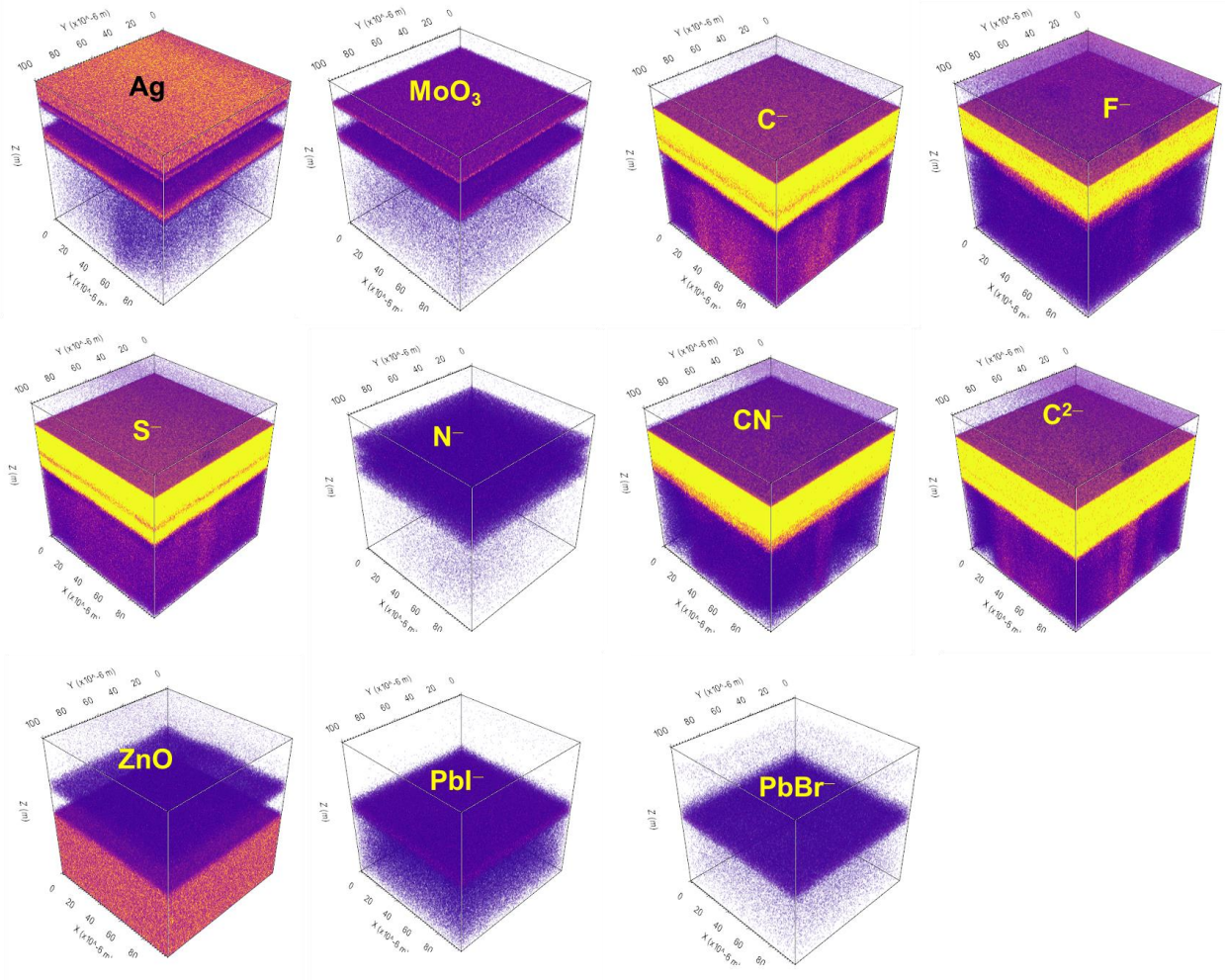

Supplementary Figure S33| 2D cross-sectional image profile of silver, MoO_3, carbon, nitrogen, ZnO, lead iodide and lead bromide elemental profile images of the γ–$CsPbI_{2.2}Br_{0.8}$-based 2T-HTSC device measured by ToF-SIMS. ToF:SIMS recorded after 20 days aging.

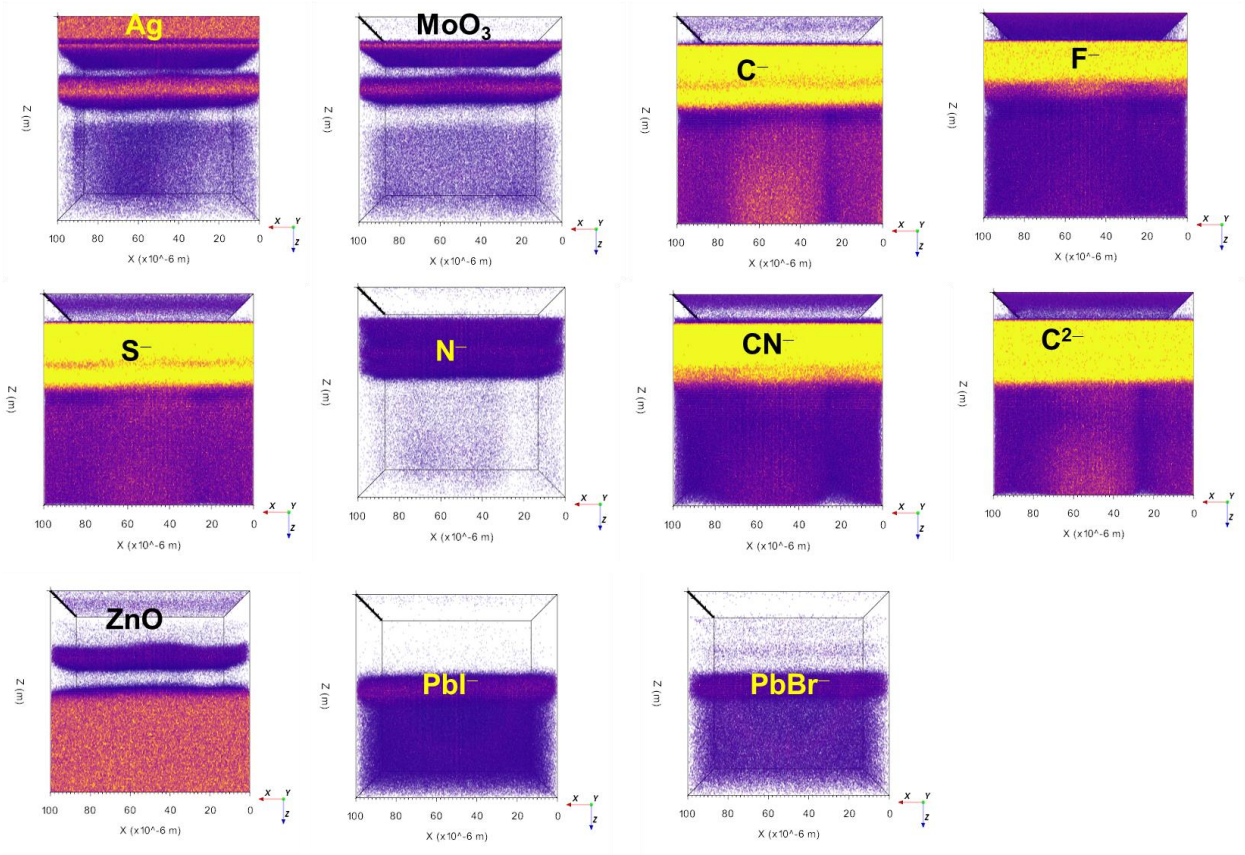

Supplementary Figure S34| ToF-SIMS depth profiles of the γ–$Cs_{0.99}Rb_{0.01}PbI_{2.2}Br_{0.8}$-based 2T-HTSC device indicating silver, MoO_3, carbon, nitrogen, ZnO, oxygen lead iodide and lead bromide elementals are distributed uniformly. Note: ToF:SIMS recorded after 20 days aging.

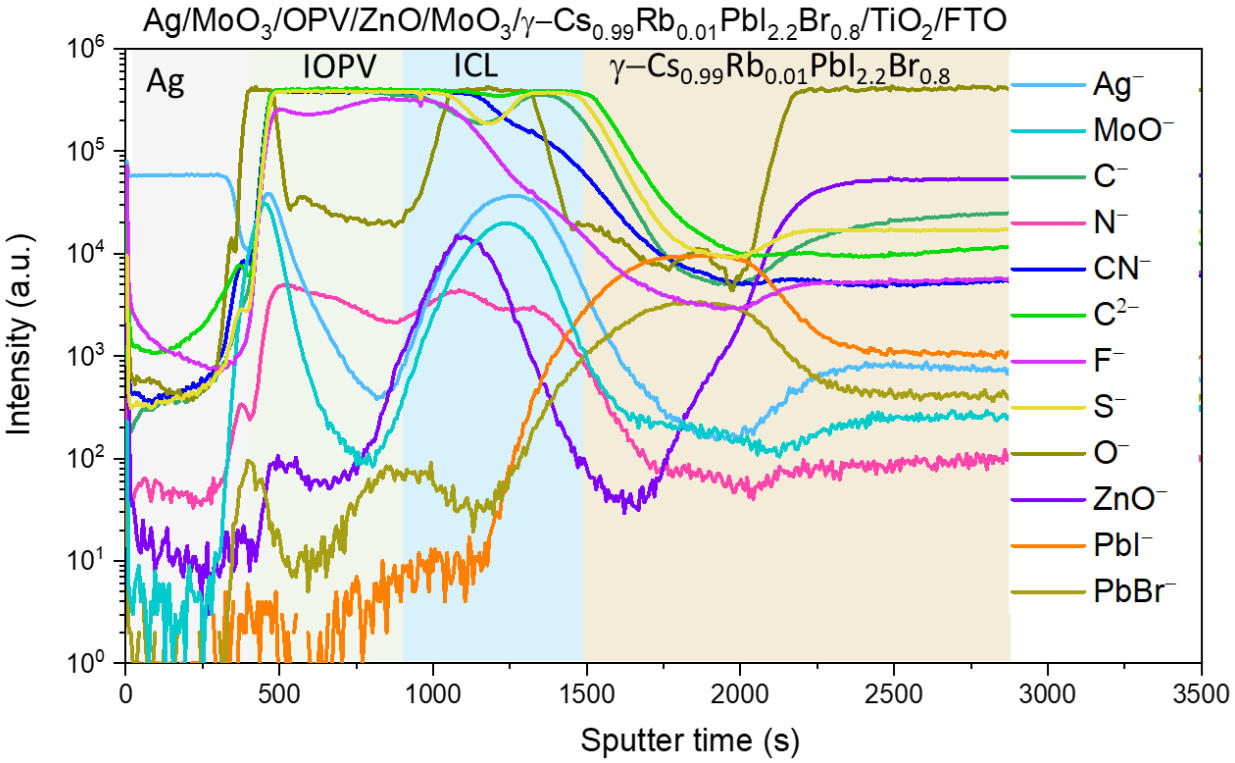

Supplementary Figure S35| Reconstructed 3D cross-sectional image profile showing separate silver, MoO_3, carbon, nitrogen, ZnO, lead iodide and lead bromide elemental layers of the γ–$Cs_{0.99}Rb_{0.01}PbI_{2.2}Br_{0.8}$-based 2T-HTSC device measured by ToF-SIMS. Note: ToF:SIMS recorded after 20 days aging.

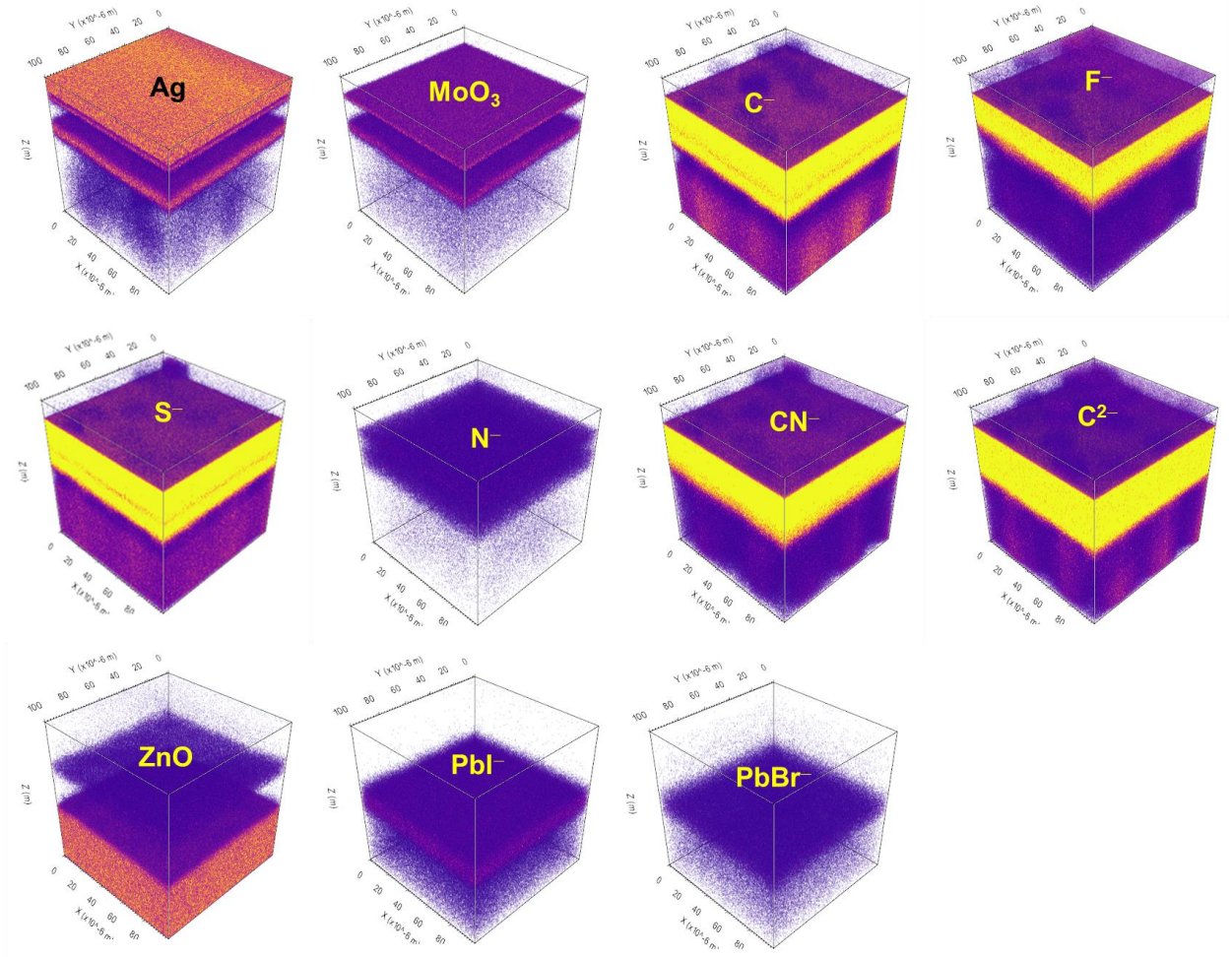

Supplementary Figure S36| 3D cross-sectional image profile of silver, MoO_3, carbon, nitrogen, ZnO, lead iodide and lead bromide elemental profile images of the γ–$Cs_{0.99}Rb_{0.01}PbI_{2.2}Br_{0.8}$-based 2T-HTSC device measured by ToF-SIMS. ToF:SIMS recorded after 20 days aging.

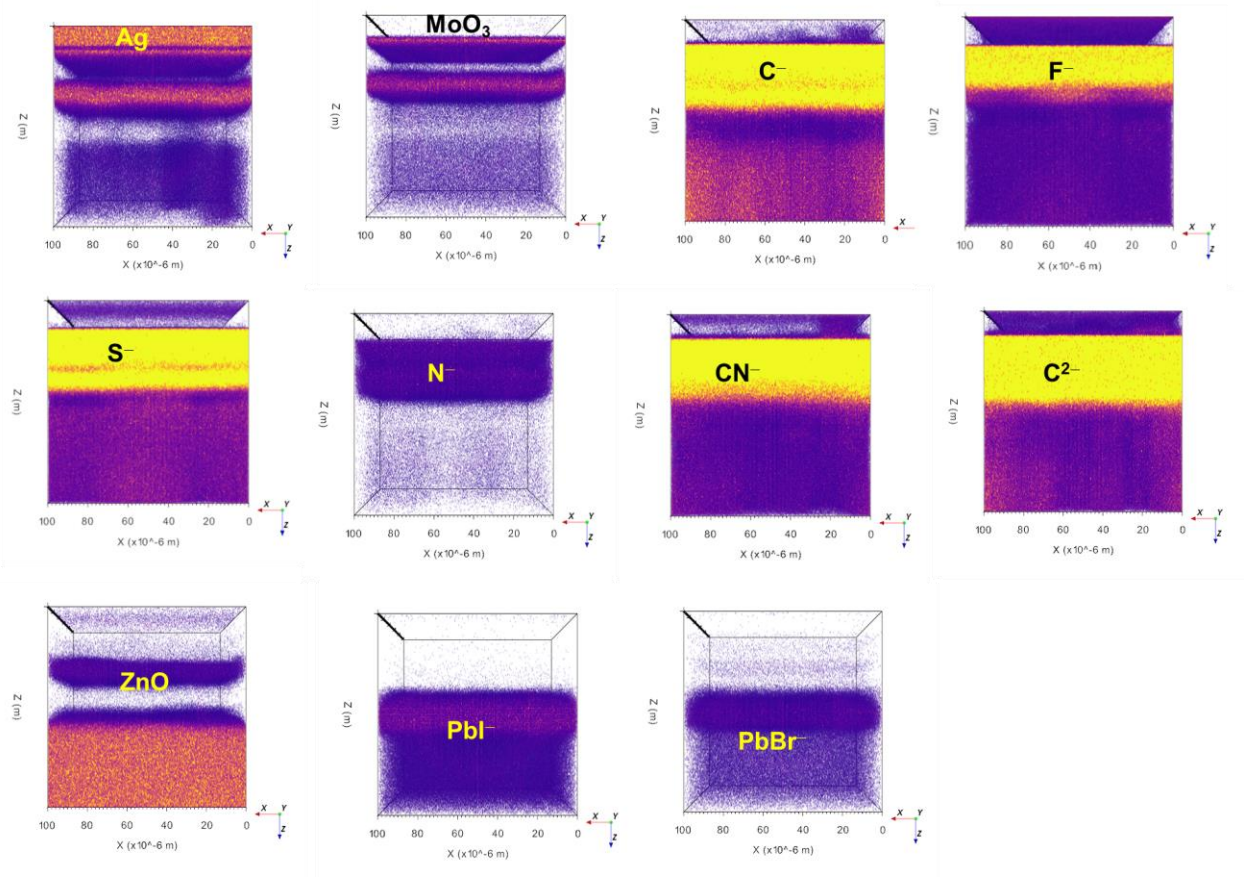

Supplementary Figure S37| a, Chlorine elemental depth profile of the γ–$CsPbI_{2.2}Br_{0.8}$, γ–$Cs_{0.99}Rb_{0.01}PbI_{2.2}Br_{0.8}$/PTACl-based 2T-HTSCs in negative polarity mode. (b) Reconstructed 3D and 2D render images indicating Cl^- is absent (c) 3D and 2D render images of γ–$Cs_{0.99}Rb_{0.01}PbI_{2.2}Br_{0.8}$/PTACl-based 2T-HTSCs indicating Cl^- is present on perovskite absorber.

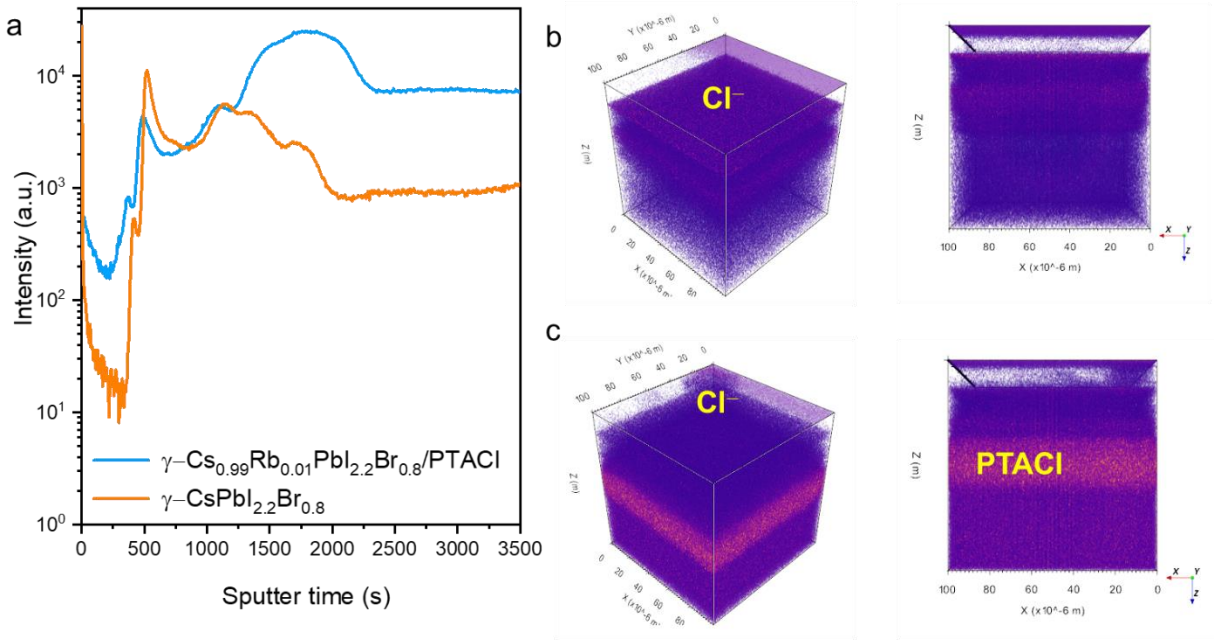

Supplementary Figure S38| J-V characteristics of metal ion doped γ–$CsPbI_{2.2}Br_{0.8}$ front subcell-based 2T-HTSCs. Rear subcells contain ternary PM6:Y6:$PC_{61}BM$ blend.

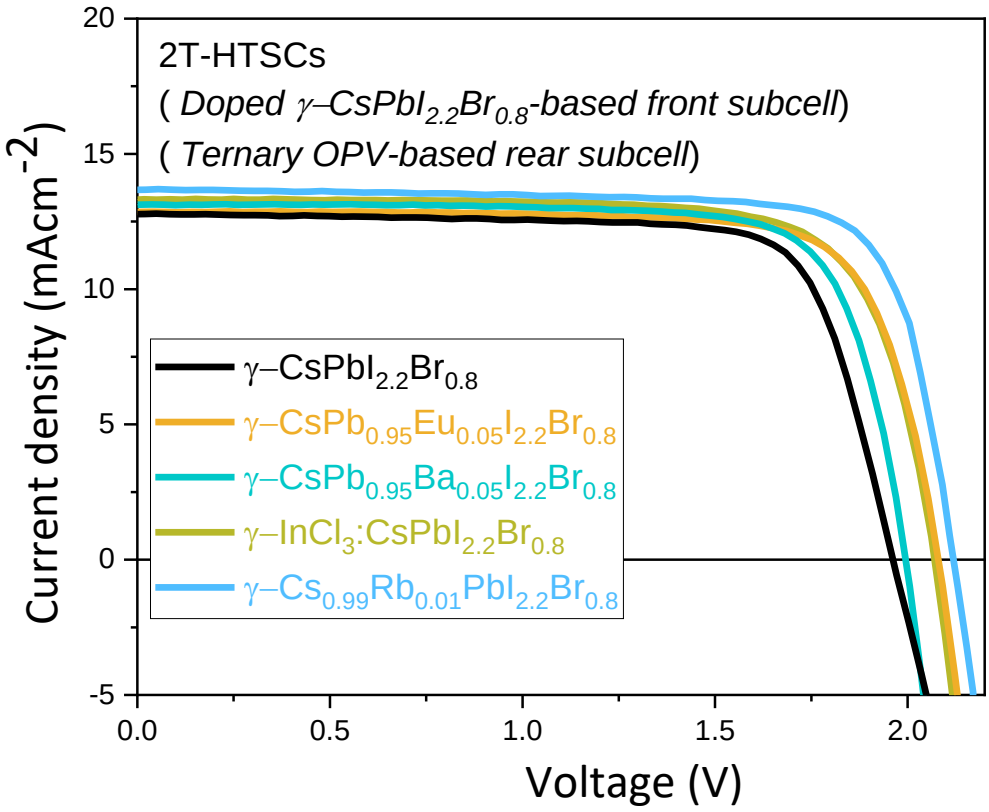

Supplementary Table S6| Summary of the performance parameters of the 2T-HTSC based on metal ion doped γ–$CsPbI_2Br$ front subcells. Front subcells contain ternary PM6:Y6:PCBM blend.

Device	**V_{OC} (V)**	**J_{SC} ($mAcm^{-2}$)**	**FF (%)**	**PCE (%)**	**V_{loss} (V)**
γ–$CsPbI_{2.2}Br_{0.8}$/PM6:Y6:PCBM	1.957	12.76	79.95	19.96	0.093
γ–$CsPb_{0.95}Ba_{0.05}I_{2.2}Br_{0.8}$/PM6:Y6:PCBM	1.994	13.08	78.5	20.47	0.096
γ–$CsPb_{0.95}Eu_{0.05}I_{2.2}Br_{0.8}$/PM6:Y6:PCBM	2.076	12.97	76.62	20.63	0.029
γ–$InCl_3$:$CsPbI_{2.2}Br_{0.8}$/PM6:Y6:PCBM	2.078	13.28	77.35	21.34	0.052
γ–$Cs_{0.99}Rb_{0.01}PbI_{2.2}Br_{0.8}$ /PM6:Y6:PCBM	2.110	13.65	80.10	23.07	0.025

Supplementary Table S3| Comparison the state-of-the-art performances of perovskite/organic tandem solar cells reported in the literature with present work.

Device Structure	PCE	J_{SC} ($mAcm^{-2}$)	V_{OC} (V)	FF (%)	V_{OC} loss (V)	Certified	Ref.
ITO/PEDOT:PSS/$MAPbI_{3-x}Cl_x$/PCBM/PFN/Step layer/MoO_3/PBDTT/$PC_{70}BM$/Ca/Al	8.62	8.02	1.58	68	0.02	N/A	S7
ITO/PEDOT:PSS/PBSeDTEG8:PCBM/PFN/TiO_2/PH500/PEDOT:PSS/ $MAPbI_3$ /PCBM/PFN/Al	10.2	10.05	1.52	67	0.07	N/A	S8
ITO/NiO/PSS/ $FAPbBr_xCl_{3+x}$/PSS/PCBM/ZnO-NP / ITO/PEDOT:PSS/PTB7-Th:6TIC-4F/ZnO-NP/ITO	10.83	6.6	2.23	74	0.04	N/A	S9
ITO/PEDOT:PSS/$MAPbI_3$/$PC_{61}BM$/MoO_3/Ag/C_{60}-SB/PCE-10:$PC_{71}BM$/C_{60}-N/Ag	16.0	13.1	1.63	75.1	0.17	N/A	S10
ITO/PTAA/$Cs_{0.1}(FA_{0.6}MA_{0.4})_{0.9}Pb(I_{0.6}Br_{0.4})_3$/PCBM/BCP/Ag/M-PEDOT/SN6IC-4F/Bis-C_{60}/BCP/Ag	15.13	11.52	1.85	70.98	0.14	N/A	S11
ITO/MeO-2PACz/$FA_{0.8}Cs_{0.2}Pb(I_{0.5}Br_{0.5})_3$/PEAI 2D/PCBM/AZO NP/SnOx/InOx/MoO_3/PM6:Y6:$PC_{61}BM$/C60/BCP/Ag	23.7	14.2	2.15	78	0.06	23.1	S12
ITO/NiOx/$FA_{0.8}MA_{0.02}Cs_{0.18}PbI_{1.8}Br_{1.2}$/$C_{60}$/BCP/Ag NP/ MoO_x/PBDBT-2F:Y6:$PC_{71}BM$/ TPBi/Ag	20.6	13.05	1.902	83.1	0.065	19.54	S13
ITO/NiO_x/BPA/$Cs_{0.25}FA_{0.75}Pb(I_{0.6}Br_{0.4})_3$/$C_{60}$/BCP/IZO/$MoO_x$/PM6:Y6:$PC_{71}BM$/PNDIT-F3N/Ag	23.6	14.83	2.06	77.2	0.042	22.94	S14
FTO/ITO/2PACz/ $FA_{0.6}MA_{0.4}Pb(I_{0.6}Br_{0.4})_3$/$C_{60}$/BCP/Ag/MoOx/PTB7-Th/BTPV-2Cl-3C9/Ag	22.0	15.7	1.88	74.6	0.02	N/A	S15
ITO/SnO_2/$CsPbI_2Br$/PTAA/ MoO_3/Au/ZnO/PTB7-Th:COi8DFIC:$PC_{71}BM$/MoO_3/Ag	15.04	11.98	1.71	73.4	0.16	N/A	S16
ITO/ZnO/SnO_2/$CsPbI_2Br$/PDCBT/MoO_3/Ag/ZnO/PM6:Y6/MoO_3/Ag	18.38	12.46	1.953	75.59	0.10	N/A	S17
ITO/ZnO/SnO_2/$CsPbI_2Br$/PDCBT/MoO_3/Ag/ZnO/PTB7-Th:O6T-4F/MoO_3/Ag	18.06	12.92	1.859	75.22		N/A	S17
ITO/ZnO/$CsPbI_2Br$/P3HT/MoOx/Au/ZnO/PTB7-Th:IEICO-4F/MoOx/Ag	18.04	12.94	1.73	81.0	0.11	N/A	S18
ITO/SnO_2/$CsPbI_2Br$/P3HT/MoO_3/Ag/PFN-Br/PTB7-Th:IEICO-4F/MoO_3/Ag	17.24	13.20	1.82		0.11	N/A	S19
ITO/SnO_2/$CsPbI_{2.1}Br_{0.9}$/PMACl/PBDB-T/MoO_3/Ag/ZnO NP/PM6:Y6/MoO_3/Ag	18.06	12.77	1.89	74.81	0.09	N/A	S20
ITO/ZnO/$CsPbI_2Br$/polyTPD/MoO_3/Ag/PFN-Br/PM6:Y6-BO/MoO_3/Ag	21.1	13.3	1.96	80.8	0.06	N/A	S21
FTO/c-TiO_2/mp-TiO_2/γ–$CsPbI_{2.2}Br_{0.8}$/PTACl/PBDB-T/MoO_3/Ag/ZnO NPs/PDIN PM6:Y6:$PC_{61}BM$/MoO_3/Ag	19.96	12.76	1.957	79.95	0.093	N/A	**This report**
FTO/c-TiO_2/mp-TiO_2/γ–$CsPb_{0.95}Ba_{0.05}I_{2.2}Br_{0.8}$/PTACl/PBDB-T/$MoO_3$/Ag/ZnO NPs/ PDIN/ PM6:Y6:$PC_{61}BM$/MoO_3/Ag	20.47	13.08	1.994	78.50	0.096	N/A	**This report**
FTO/c-TiO_2/mp-TiO_2/γ–$CsPb_{0.95}Eu_{0.05}I_{2.2}Br_{0.8}$/PTACl/PBDB-T/$MoO_3$/Ag/ZnO NPs/ PDIN/ PM6:Y6:$PC_{61}BM$/MoO_3/Ag	20.63	12.97	2.076	76.62	0.029	N/A	**This report**
FTO/c-TiO_2/mp-TiO_2/γ–$InCl_3$:$CsPbI_{2.2}Br_{0.8}$/PTACl/PBDB-T/MoO_3/Ag/ZnO NPs/ PDIN/ PM6:Y6:$PC_{61}BM$/MoO_3/Ag	21.34	13.28	2.078	77.35	0.052	N/A	**This report**
FTO/c-TiO_2/mp-TiO_2/γ–$Cs_{0.99}Rb_{0.01}PbI_{2.2}Br_{0.8}$/PTACl/PBDB-T/$MoO_3$/Ag /ZnO NPs PDIN/PM6:Y6:$PC_{61}BM$/MoO_3/Ag	23.07	13.65	2.110	80.10	0.025	N/A	**This report**

Supplementary Figure S39| Details of the statistical PV parameters of the 2T-HTCs-based on different metal ion dopants.

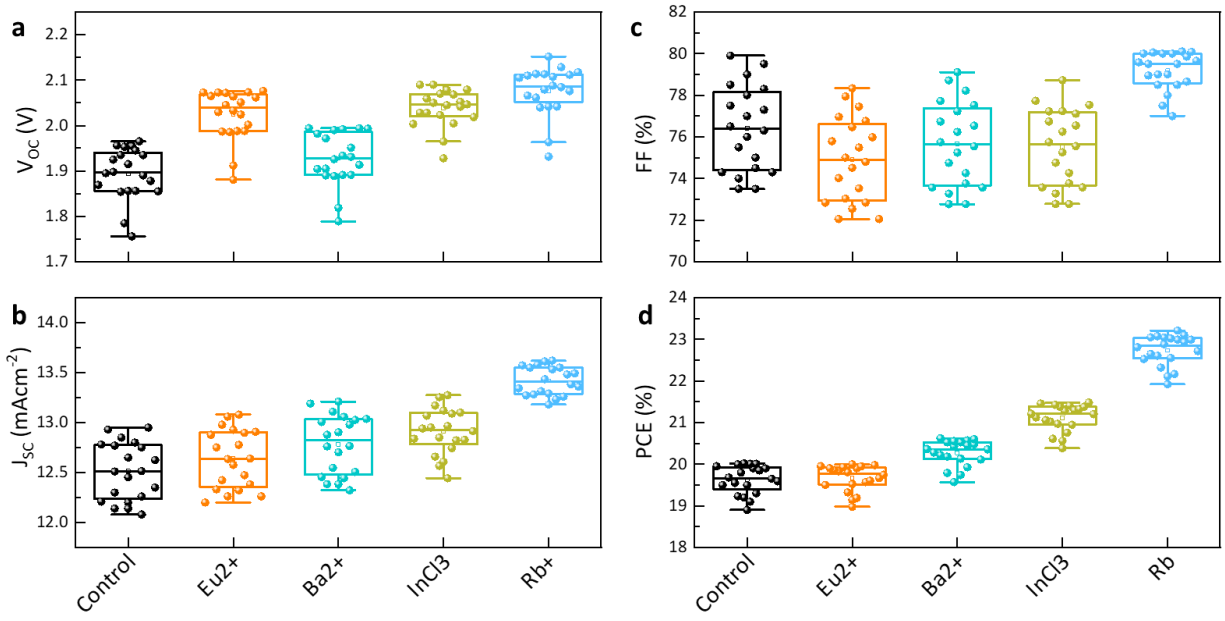

Supplementary Figure S40. Ultraviolet-photoelectron spectroscopy (UPS) spectra (using the He−I line with a photon energy of 21.22 eV). **a**. Survey spectra of γ-$CsPbI_{2.2}Br_{0.8}$-based perovskite thin films deposited using Ba^{2+}, Eu^{2+}, In^{3+} and Rb^{+} dopants. **b-f**. VBM onsets for perovskites were determined from semi-log plots. **g**. corresponding to the secondary electron onset region (WF, work function) and valence band region (VBM, valence band minimum) of the device-containing layers with respect to the Fermi energy (w.r.t. EF). **h**. Energy band levels of the device-containing layers. The dashed magenta lines indicate the work function (WF) ϕ position from vacuum level (E_{vac}) for the perovskite respective absorbers.

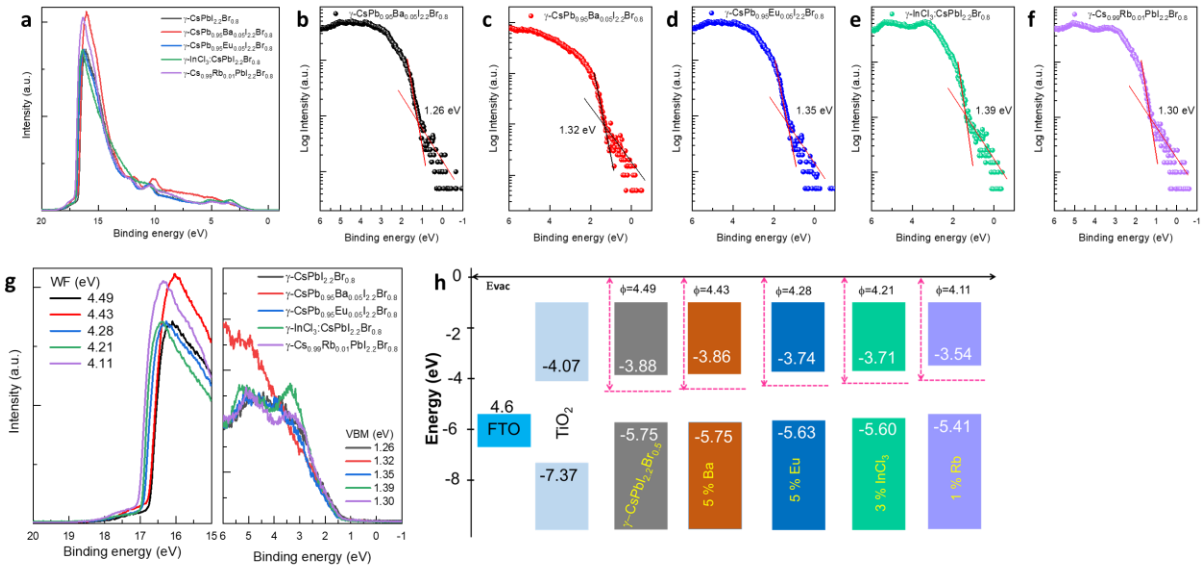

Supplementary Note S3: UPS discussion

In order to investigate the influence of Ba^{2+}, Eu^{2+}, In^{3+} and Rb^{+} dopants on their electronic structures, we obtained UPS spectra of γ-$CsPbI_{2.2}Br_{0.8}$, γ-$CsPb_{0.95}Ba_{0.05}I_{2.2}Br_{0.8}$, γ-$CsPb_{0.95}Ba_{0.05}I_{2.2}Br_{0.8}$, γ-$CsPb_{0.95}Eu_{0.05}I_{2.2}Br_{0.8}$, γ-$InCl_3$:$CsPbI_{2.2}Br_{0.8}$, and γ-$Cs_{0.99}Rb_{0.01}PbI_{2.2}Br_{0.8}$ perovskite films, **Figure S40**a. The work functions (WF) and valence band maximum (VBM) were calculated from the binding energy cut-off and the binding energy onset. The WF for each layer was estimated to be -4.49, 4.43, 4.28, 4.21 and 4.11 eV for γ-$CsPbI_{2.2}Br_{0.8}$, γ-$CsPb_{0.95}Ba_{0.05}I_{2.2}Br_{0.8}$, γ-$CsPb_{0.95}Ba_{0.05}I_{2.2}Br_{0.8}$, γ-$CsPb_{0.95}Eu_{0.05}I_{2.2}Br_{0.8}$, γ-$InCl_3$:$CsPbI_{2.2}Br_{0.8}$, and γ-$Cs_{0.99}Rb_{0.01}PbI_{2.2}Br_{0.8}$ respectively, **Fig. S40g**. We observed after Rb^{+} doping, the WF shifted upward by 380 meV (γ-$Cs_{0.99}Rb_{0.01}PbI_{2.2}Br_{0.8}$), which is much higher than other dopant. We observed 60, 210, 280 and 230 meV shifted upward towards the conduction band minimum (CBM) respectively for γ-$CsPb_{0.95}Ba_{0.05}I_{2.2}Br_{0.8}$, γ-$CsPb_{0.95}Ba_{0.05}I_{2.2}Br_{0.8}$, γ-$CsPb_{0.95}Eu_{0.05}I_{2.2}Br_{0.8}$, and γ-$InCl_3$:$CsPbI_{2.2}Br_{0.8}$ with respect to the γ-$CsPbI_{2.2}Br_{0.8}$ samples, **Fig. S40h**. These results indicate the presence of additional charge carriers after the use of these dopants. Interestingly, we observed an increased from −3.88 to −3.54 eV for the CBM and from −5.75 to −5.41 eV for the VBM for the γ-$Cs_{0.99}Rb_{0.01}PbI_{2.2}Br_{0.8}$ sample, yielding much higher gradient energy levels than rest of the samples. Therefore, a built-in band alignment within the γ-$Cs_{0.99}Rb_{0.01}PbI_{2.2}Br_{0.8}$ perovskite film

is prominent, leading to effective internal charge separation and transfer from the top interconnecting layer and the bottom electron transporting layer. This Rb^+ doping (A-site) led to a favorable energy-level alignment of the CBM between ETL and ICL than rest samples. Furthermore, this this improved energy level alignment between CBM and ICL after Rb^+ doping facilitates gradient energy levels. Therefore, we conclude that the presence of an energy gradient within the perovskite film through this Rb^+ doping is more beneficial for the favorable energetic alignment at the front subcell/ICL interface, which is responsible for the increased V_{OC} and other photovoltaic properties of the Rb-based 2T-HTSCs.

Supplemental Table S7. Calculated parameters for energy levels of γ-$CsPbI_{2.2}Br_{0.8}$-based perovskite thin films deposited using Ba^{2+}, Eu^{2+}, In^{3+} and Rb^+ dopants from UPS analysis.

Sample	E_{cutoff} (eV)	WF (ϕ) (eV)	VBM-E_F (eV)	VBM (eV)	ΔE_g (eV)	CBM (eV)
γ-$CsPbI_{2.2}Br_{0.8}$	16.73	4.49	1.26	5.75	1.87	3.88
γ-$CsPb_{0.95}Ba_{0.05}I_{2.2}Br_{0.8}$	16.79	4.43	1.32	5.75	1.89	3.86
γ-$CsPb_{0.95}Eu_{0.05}I_{2.2}Br_{0.8}$	16.94	4.28	1.35	5.63	1.89	3.74
γ-$InCl_3$:$CsPbI_{2.2}Br_{0.8}$	17.01	4.21	1.39	5.60	1.89	3.71
γ-$Cs_{0.99}Rb_{0.01}PbI_{2.2}Br_{0.8}$	17.11	4.11	1.30	5.41	1.87	3.54

Supplementary Figure S41| J–V curves (reverse and forward scans) of the control small-area (0.09 cm^2) all-inorganic perovskite/IOPV 2T-HTSC.

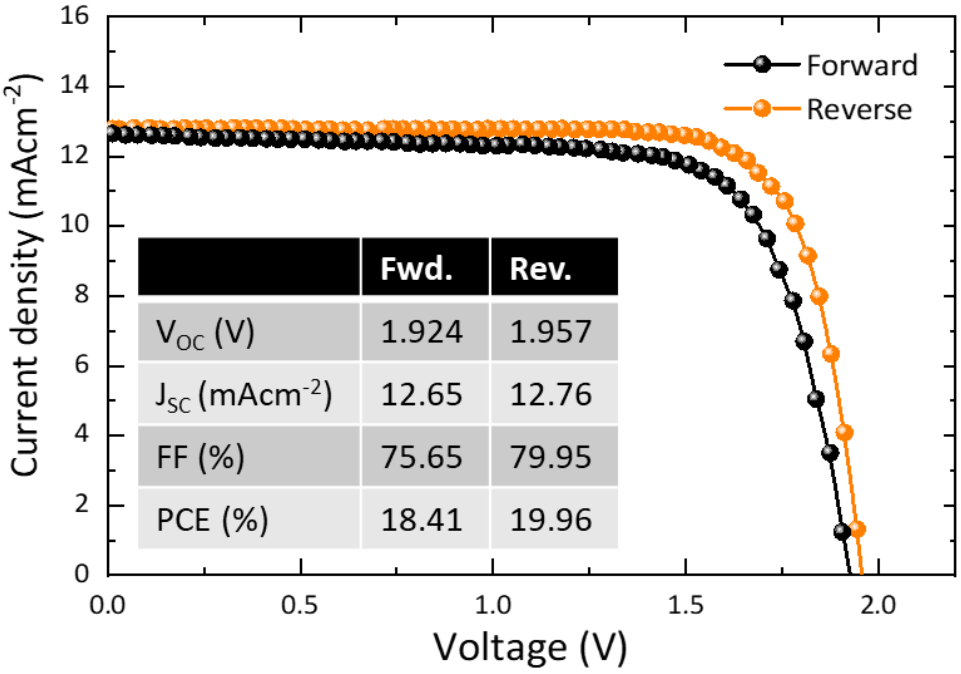

	Fwd.	Rev.
V_{OC} (V)	1.924	1.957
J_{SC} (mAcm^{-2})	12.65	12.76
FF (%)	75.65	79.95
PCE (%)	18.41	19.96

Supplementary Figure S42| Photovoltaic characteristics. SPO analysis of all champion small-area 2T-HSCs under AM 1.5G illumination (100 mWcm^{-2}).

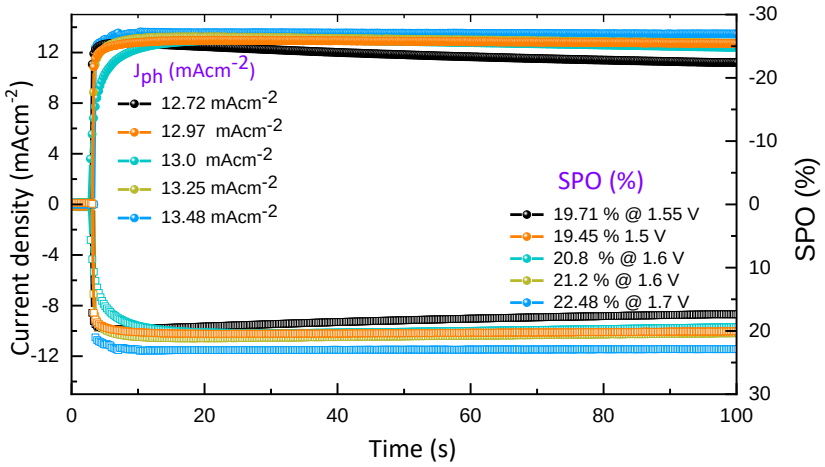

Supplementary Figure S43| Shelf-life stability of the 2T-HTSCs based on different metal ion doped front subcells and ternary PM6:Y6:$PC_{61}BM$ rear subcells. The devices without encapsulation were kept at room temperature in dry box Relative humidity inside dry box was ~10 %. Samples were taken outside for J-V analysis and immediately stored in dry box. *Note: HTSCs are much stable than single front subcells due to OPV blend layer itself acts as encapsulation layer for front subcells.*

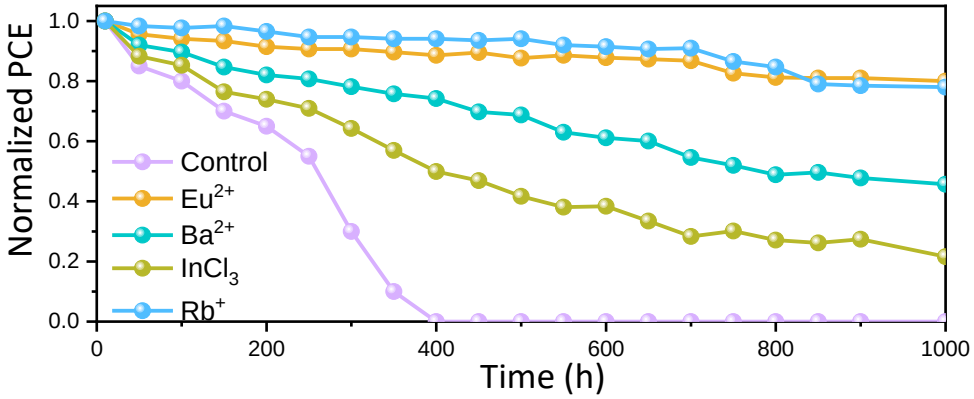

Supplementary Figure S44| Stability of single subcells and 2T-HTSCs monitored 5 mWcm^{-2} 365 nm UV light continuous illumination at room temperature.

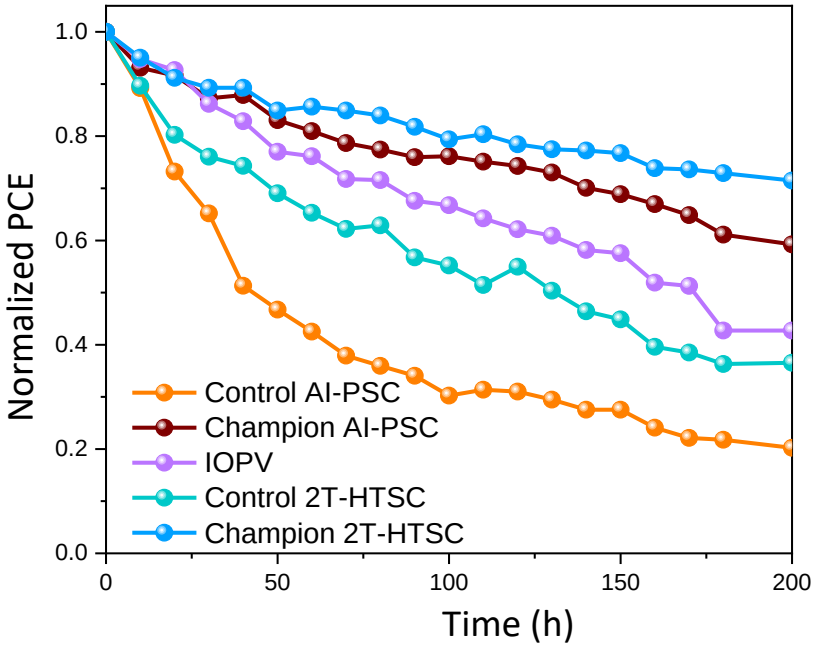

Supplementary Figure S45| Experimental setup for stability analysis in ambient condition. Operational stability of the champion large area perovskite/organic tandem solar cell under 1 sun LED illumination (100 mW/cm^2).

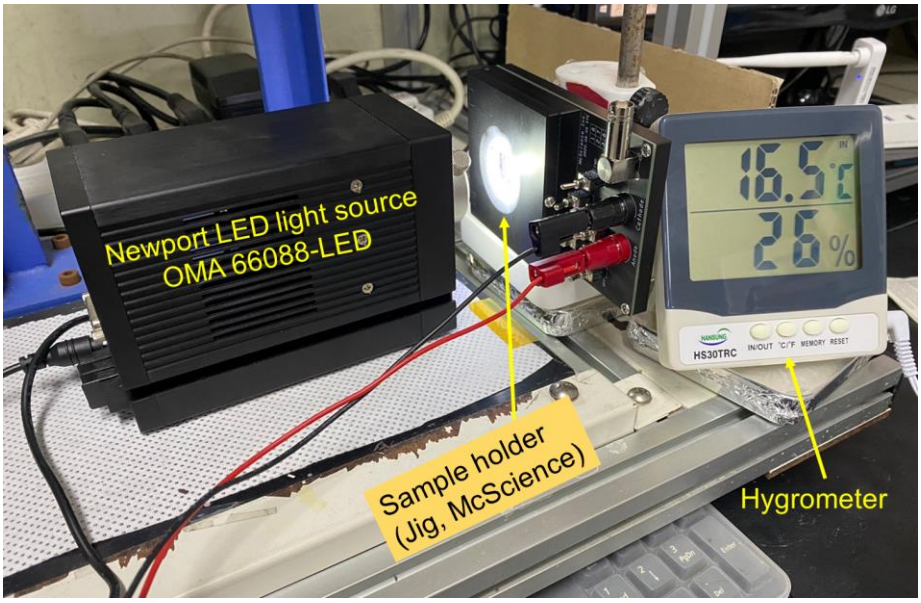

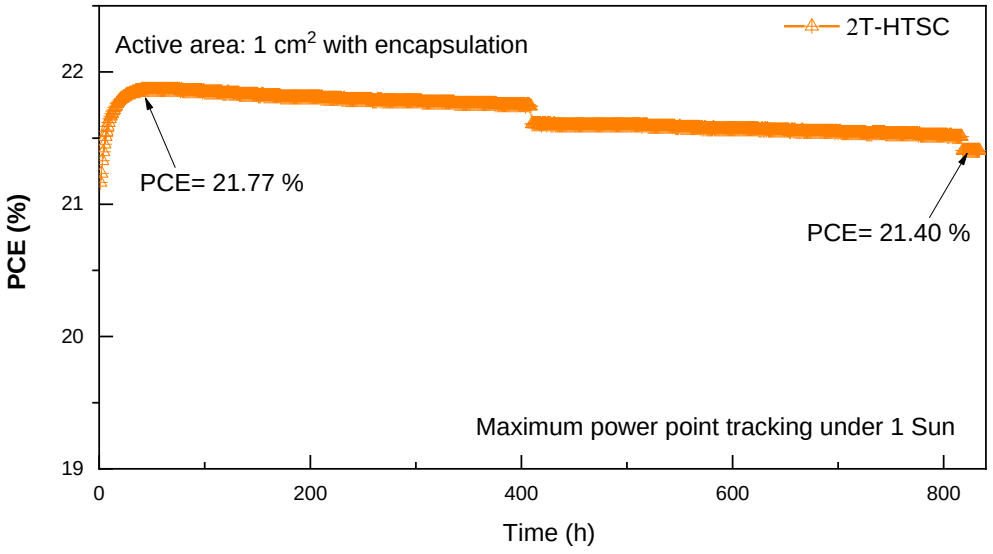

Supplementary Figure S46| Thermal stability analysis. Thermal stability tests of the 2T-HTSCs at 65 °C **a;** and 85 °C **b**; thermal stress. All types of devices were encapsulated with PDMS (Syngard 184 Simicone Elastomer) and stored at N_2 filled glove box on the hot plate at respective temperature. For J-V measurements devices were taken outside the glove box (every ~24 h) and immediately kept in glove box after J-V measurements every. *Note: All-inorganic perovskite layers are more stable at 65°C and 85 °C thermal stress than room temperature.*

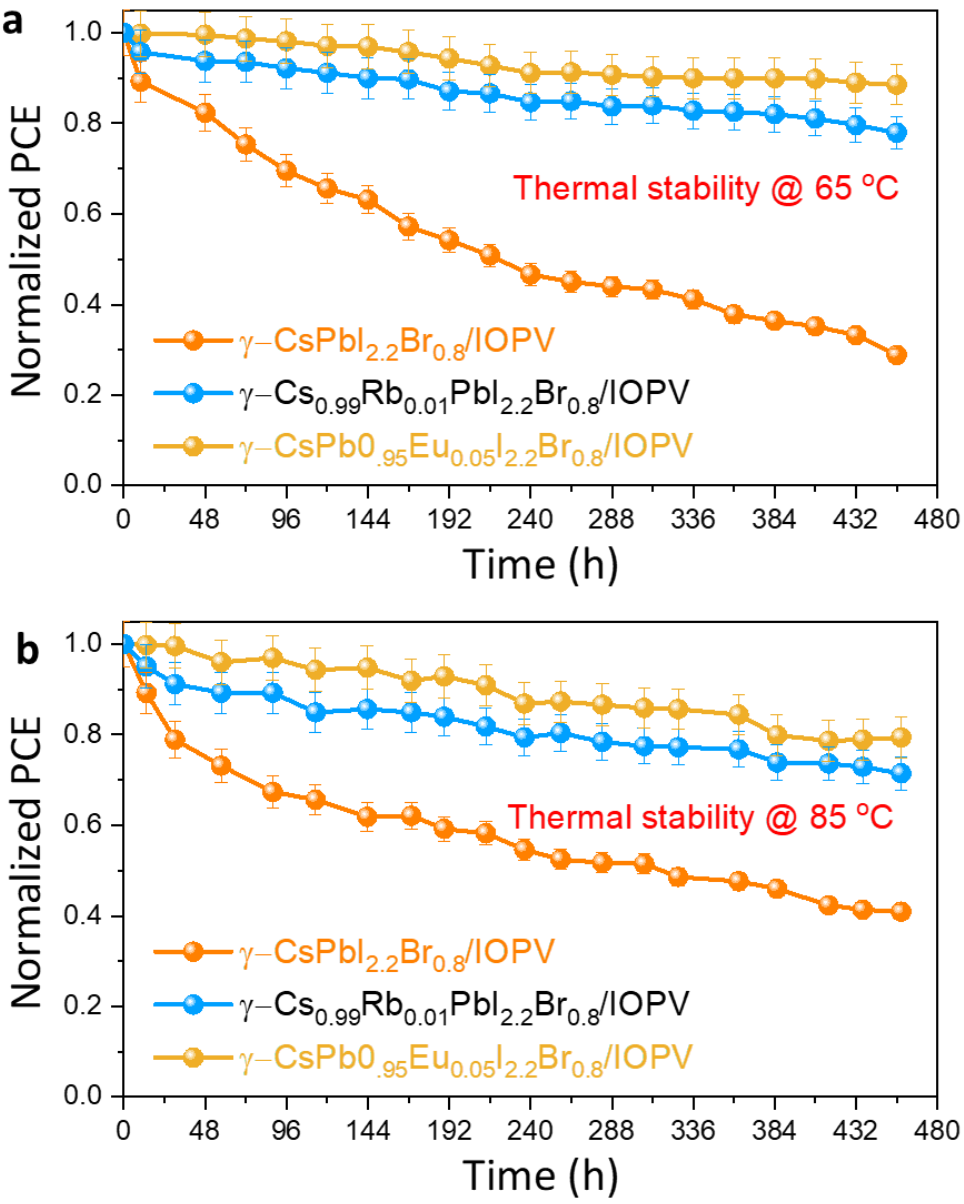

Supporting references:

[S1] R. Lin, K. Xiao, Z. Qin, Q. Han, C. Zhang, M. Wei, M. I. Saidaminov, Y. Gao, J. Xu, M. Xiao, A. Li, J. Zhu, E. H. Sargent and H. Tan, *Nat. Energy*, 2019, **4**, 864–873.

[S2] S.S. Mali, J.V. Patil, P. S. Shinde, G. de Migul and C. K. Hong, *Matter,* 2021, **4(2)**, 635-653.

[S3] https://pubchem.ncbi.nlm.nih.gov/compound/3555371

[S4] J.A. Steele, E. Solano, H. Jin, V. Prakasam, T. Braeckevelt, H. Yuan, Z. Lin, R. de Kloe, Q. Wang, S. M. J. Rogge, V. Van Speybroeck, D. Chernyshov, J. Hofkens, and M. B. J. Roeffaers, *Adv. Mater.*, 2021, **33**, 2007224.

[S5] J. Rodríguez-Carvajal, *Physica B: Condensed Matter,* 1993, **192**, 55-69.

[S6] J. A. Steele, V. Prakasam, H. Huang, E. Solano, D. Chernyshov, J. Hofkens and M. B. J. Roeffaers. *J. Am. Chem. Soc.,* 2021, **143(28)**, 10500–10508.

[S7] J. Liu, S. Lu, L. Zhu, X. Li and W. C. H. Choy, *Nanoscale*, 2016**, 8**, 3638-3646.

[S8] C.-C. Chen, S.-H. Bae, W.-H. Chang, Z. Hong, G. Li, Q. Chen, H. Zhou and Y. Yang, *Mater. Horiz.*, 2015, **2**, 203-211.

[S9] L. Zuo, X. Shi, W. Fu and A. K.-Y. Jen, *Adv. Mater.*, 2019, **31**, 1901683.

[S10] Y. Liu, L. A. Renna, M. Bag, Z. A. Page, P. Kim, J. Choi, T. Emrick, D. Venkataraman and T. P. Russell, *ACS Appl. Mater. Interfaces*, 2016, **8**, 7070-7076.

[S11] Z. Li, S. Wu, J. Zhang, K. C. Lee, H. Lei, F. Lin, Z. Wang, Z. Zhu and A. K. Y. Jen, *Adv. Energy Mater.*,2020, **10**, 2000361.

[S12] K. Brinkmann, T. Becker, F. Zimmermann, C. Kreusel, T. Gahlmann, M. Theisen, T. Haeger, S. Olthof, C. Tückmantel, M. Günster, T. Maschwitz, F. Göbelsmann, C. Koch, D. Hertel, P. Caprioglio, F. Peña-Camargo, L. Perdigón-Toro, A. Al-Ashouri, L. Merten, A. Hinderhofer, L. Gomell, S. Zhang, F. Schreiber, S. Albrecht, K. Meerholz, D. Neher, M. Stolterfoht and T. Riedl, *Nature,* 2022, **604**, 280–286.

[S13] X. Chen, Z. Jia, Z. Chen, T. Jiang, L. Bai, F. Tao, J. Chen, X. Chen, T. Liu, X. Xu, C. Yang, W. Shen, W. E.I. Sha, H. Zhu and Y. Yang, *Joule*, 2020, **4**, 1594-1606.

[S14] W. Chen, Y. Zhu, J. Xiu, G. Chen, H. Liang, S. Liu, H. Xue, E. Birgersson, J. W. Ho, X. Qin, J. Lin, R. Ma, T. Liu, Y. He, A. M.-C. Ng, X. Guo, Z. He, H. Yan, A. B. Djurišić and Y. Hou, *Nat. Energy*, 2022, **7**, 229–237.

[S15] S. Qin, C. Lu, Z. Jia, Y. Wang, S. Li, W. Lai, P. Shi, R. Wang, C. Zhu, J. Du, J. Zhang, L. Meng and Y. Li, *Adv. Mater.*, 2022, **34**, 2108829.

[S16] Q. Zeng, L. Liu, Z. Xiao, F. Liu, Y. Hua, Y. Yuan and L. Ding, *Sci. Bull.*, 2019, **64(13)**, 885-887.

[S17] S. Xie, R. Xia, Z. Chen, J. Tian, L. Yan, M. Ren, Z. Li, G. Zhang, Q. Xue, H.-L. Yip and Y. Cao, *Nano Energy*, 2020, **78**, 105238.

[S18] H. Aqoma, I. F. Imran, F. T. A. Wibowo, N. V. Krishna, W. Lee, A. K. Sarker, D. Y. Ryu and S.-Y. Jang, *Adv. Energy Mater.*, 2020, **10(37)**, 2001188.

[S19] K. Lang, Q. Guo, Z. He, Y. Bai, J. Yao, M. Wakeel, M. S. Alhodaly, T. Hayat and Z. Tan, *J. Phys. Chem. Lett.*, 2020, **11(22)**, 9596.

[S20] X. Wu, Y. Liu, F. Qi, F. Lin, H. Fu, K. Jiang, S. Wu, L. Bi, D. Wang, F. Xu, A. K.-Y. Jen and Z. Zhu, *J. Mater. Chem.* A, 2021, **9**, 19778.

[S21] P. Wang, W. Li, O. J. Sandberg, C. Guo, R. Sun, H. Wang, D. Li, H. Zhang, S. Cheng, D. Liu and J. Min, *Nano Lett.*, 2021, **21(18)**, 7845–7854.